GEOLOGICA CARPATHICA, FEBRUARY 2023, 74, 1, 3–21 https://doi.org/10.31577/GeolCarp.2023.04

Genesis of a synmagmatic charnockite associated with the Weinsberg granite, southern Bohemian Batholith, northern Austria

DANIEL HARLOV[1,2,3,✉], ALFONS VAN DEN KERKHOF[4], BRUNO HAUNSCHMIDT[5] and FRIEDRICH FINGER[5]

[1]Deutsches GeoForschungsZentrum – GFZ, Telegrafenberg, 14473 Potsdam, Germany; ✉dharlov@gfz-potsdam.de
[2]Faculty of Earth Resources, China University of Geosciences, Wuhan 430074, China
[3]Department of Geology, University of Johannesburg P.O. Box 524, Auckland Park, 2006 South Africa
[4]Geowissenschaftliches Zentrum der Universität Göttingen, Goldschmidtstrasse 3, 37077 Göttingen, Germany
[5]Department of Environment & Biodiversity, University of Salzburg, Hellbrunnerstrasse 34, 5020 Salzburg, Austria

(Manuscript received September 12, 2022; accepted in revised form January 19, 2023; Associate Editor: Igor Broska)

Abstract: The Weinsberg granite, a coarse-grained biotite granite with abundant K-feldspar megacrystals, is the volumetrically dominant and most characteristic granite type of the late-Variscan Moldanubian Batholith in the Moldanubian zone of the Bohemian Massif. In the western batholith area, a local orthopyroxene-bearing variant (charnockite) of the Weinsberg granite has been identified and given the name of the Sarleinsbach quartz-monzodiorite in previous studies. Whole rock analysis of the charnockite and the relatively mafic Weinsberg granite in the immediate neighborhood show no significant geochemical differences with respect to either the major or trace elements. The mineralogy and petrology of the charnockite and surrounding granite are the same except for the presence of orthopyroxene ±clinopyroxene in the charnockite. In addition, the charnockite is characterized by the presence of dark grey, glassy orthoclase megacrysts with only some partial conversion to microcline, whereas in the granite the K-feldspar megacrysts consist of white microcline. The Fe–Mg silicates in the charnockite (orthopyroxene, clinopyroxene, amphibole, and biotite) are relatively Fe-rich (X_{Fe}=0.6–0.7) whereas the plagioclase is more albitic (X_{Ab}=0.6) than anorthitic. Fluid inclusions from the granite and associated charnockite are investigated and the results compared. The basic conclusion is that the magma responsible for the granite was dominated by an H_2O-rich fluid with a $CaCl_2$ component. The magma responsible for the charnockite was dominated by a CO_2-rich fluid with a minor NaCl component, which lowered the H_2O activity sufficiently below 1 such that orthopyroxene ±clinopyroxene was the stable Fe–Mg silicate phase during crystallization as opposed to the biotite in the granite. Taking into account that CO_2-rich and H_2O-rich fluids are immiscible in the presence of NaCl and $CaCl_2$ over the P–T range of the overall crust, the implication is that in granitoid melts, if CO_2 is present, there will be regions dominated by CO_2 and regions dominated by H_2O. The extent of either region will be determined by the overall CO_2/H_2O ratio in the melt. In the CO_2-dominated regions, the H_2O activity could be sufficiently lowered such that orthopyroxene is the stable Fe–Mg silicate phase during crystallization, though this will also be dependent on the Fe/Mg ratio of these phases and the overall whole rock chemistry of the melt. In addition to incipient solid state charnockitization, commonly seen in the Archean terranes of southern India and elsewhere, this suggests that a certain subset of granites and granitoids worldwide should have patches and/or limited areas of charnockite if the amount of CO_2 present in the original magma goes above a certain fraction.

Keywords: Weinsberg granite, Sarleinsbach quartz-monzodiorite, charnockite, CO_2, NaCl–KCl–$CaCl_2$, fluid inclusions, orthopyroxene

Introduction

The genesis, emplacement, and subsequent evolution of igneous granitoid intrusions is a topic that has excited much discussion over the last 100 years or so (see reviews in Clemens (2012) and Brown (2013)). One of the focuses of this discussion has been on the role of fluids during this process from inducing initial melting in the source rock and/or sediments to the final disposition of these fluids during the crystallization of the granitoid body. The fluids normally found associated with a granitoid melt consist primarily of H_2O, CO_2, and NaCl-, KCl-, and $CaCl_2$-bearing saline fluids (Brown 2013; Manning 2018). Normally H_2O is the dominant component in the fluid phase such that the H_2O activity is equal to or greater than 1, or approaches 1 during magmatic crystallization. In such cases the Fe–Mg silicates crystallizing out with the granite will be biotite and/or amphibole. In cases where the H_2O activity is sufficiently below 1, orthopyroxene±clinopyroxene will become the stable Fe–Mg silicate phases crystallizing out via the reactions:

$$\underset{\text{biotite}}{K(Fe,Mg)_3AlSi_3O_{10}(OH)_2} + 3\,\underset{\text{quartz}}{SiO_2} = 3\,\underset{\text{orthopyroxene}}{(Fe,Mg)SiO_3} + \underset{\text{K-feldspar}}{KAlSi_3O_8} + H_2O \quad (1)$$

and:

$$\underset{\text{hornblende}}{KCa_2(Fe,Mg)_4Al_3Si_6O_{22}(OH)_2} + 4\,\underset{\text{quartz}}{SiO_2} =$$
$$= \underset{\text{clinopyroxene}}{Ca(Fe,Mg)Si_2O_6} + 3\,\underset{\text{orthopyroxene}}{(Fe,Mg)SiO_3} + \underset{\text{plagioclase}}{CaAl_2Si_2O_8} + \underset{\text{K-feldspar}}{KAlSi_3O_8} + H_2O \quad (2)$$

A low H_2O activity generally implies an increase in the relative amounts of CO_2 and/or a NaCl–KCl–$CaCl_2$ relative to H_2O in the fluid associated with the melt (cf. Frost et al. 2000; Frost & Frost 2008; Manning 2018).

Modal mineral variations in a granite are normally attributed to whole-rock geochemical variability. Fluid inclusion studies have been made of granitoid rocks and used to infer the existence of the co-existing fluid. In most of these cases these fluids are dominated by H_2O though there are cases where CO_2 has been demonstrated to be the dominant fluid such as in the case of the Varberg charnockite (Harlov et al. 2013, 2014) and the Wind River charnockite (Frost et al. 2000) where orthopyroxene is the dominant Fe–Mg silicate as opposed to biotite and amphibole. In either case, the inference is that these magmatic charnockites formed in a CO_2-rich environment.

In this study, we report a case where the activity of H_2O is a major factor in the occurrence of biotite vs. orthopyroxene despite the fact that both the charnockite and associated granite have identical whole rock compositions and the same age. The charnockite in question, known in previous studies as the orthopyroxene-bearing Sarleinsbach quartz-monzodiorite, is associated with the Variscan age 323 Ma Weinsberg granite in the Sarleinsbach area of northern Austria. We use this particular example to discuss whether or not the presence of CO_2-rich fluid inclusions can be used to infer a high CO_2 content in the magmatic granitoid system and the role a high CO_2 content plays in determining the H_2O activity of the system with respect to the stability of orthopyroxene relative to biotite and amphibole in this system.

Geological background

Weinsberg granite

The Weinsberg granite, a coarse-grained biotite granite with abundant K-feldspar megacrystals, is the volumetrically dominant and most characteristic granite type of the late-Variscan Moldanubian Batholith in the Moldanubian zone of the Bohemian Massif (Fig. 1). Together with other granite varieties (coarse and fine-grained two-mica granite, fine-grained biotite granite) it covers an area of more than 1000 km^2 in the Austrian, Czech, and Bavarian sectors of the batholith. ID-TIMS zircon dating by Gerdes (2001) has shown that the Weinsberg granite intruded in several steps between 330.7 ± 0.4 Ma and 322.5 ± 0.5 Ma (Fig. 1A).

The Weinsberg granite is interpreted to have been a hot lower crustal magma that formed through the fluid-absent dehydration melting of heterogeneous, high-K, biotite-bearing, lower-crustal source rocks (Finger & Clemens 1995, 2002; Finger et al. 2003). Many samples of Weinsberg granite are metaluminous to slightly peraluminous (A/CNK 0.98–1.1), which hints at an igneous source (biotite tonalite or granodiorite) rather than a metasedimentary source. However, some variants of Weinsberg granite are slightly more peraluminous (A/CNK ~ 1.10–1.15) and tend towards the S-type (melting of a metasedimentary lower crust).

In the western batholith area, a local body of the Weinsberg granite has been mapped out (Frasl & Finger 1988; Haunschmid & Finger 1994; Klötzli et al. 2001) (Fig. 1B). It contains orthopyroxene-bearing regions (charnockite) that have been summarized as the Sarleinsbach quartz-monzodiorite by Frasl & Finger (1988). Finger & Clemens (1995, 2002) proposed that the Sarleinsbach quartz-monzodiorite represents a local cumulative magma, whose crystallization started within the orthopyroxene P–T stability field under granulite-facies conditions. The magma itself was a product of partial melting of heterogeneous, high-K, biotite-bearing, lower crustal sources.

Sarleinsbach quartz-monzodiorite (charnockite)

The orthopyroxene-bearing (charnockite) Sarleinsbach quartz-monzodiorite is exposed in a series of outcrops SW of Rohrbach between Saleinsbach and Arnreith (Fig. 1B). Compared to the main body of the Weinsberg granite, it is characterized by the presence of orthopyroxene ± clinopyroxene (Fig. 2). The contact between the charnockite and the non-orthopyroxene-bearing surrounding Weinsberg granite for extremely coarse-grained rocks can be sharp (primary or tectonic, e.g. outcrop south of Arnreith) or, more often, appear to be transitional (Fig. 2C, D, E). The smallest, observable charnockite domains are about 1 meter in size and angular in shape. The maximum size of the charnockite domains is some hundreds of meters. Unfortunately, there is no large, continuous, fresh outcrop where one could observe the actual size of the largest charnockite domains within the Weinsberg granite. The relatively indistinguishable nature of the charnockite from the surrounding, often relatively mafic granite in weathered outcrops has resulted in the fact that the rock type was only discovered in 1983 (by G. Frasl) and has not yet been mapped out in detail though some attempt was made by Klötzli et al. (2001) from whom Figure 1B is taken. The slightly darker appearance of the charnockite, in comparison to the surrounding granite, is mainly due to the large, semi-transparent, grey orthoclase phenocrysts. In contrast, the surrounding Weinsberg granite contains milky-white microcline (compare Fig. 2A and 2B).

Analytical technique

Sample selection

Fresh samples of both the Weinsberg granite and associated orthopyroxene-bearing (charnockite) Sarleinsbach quartz-monzodiorite were selected from a variety of locations. Polished thin sections were prepared from all samples

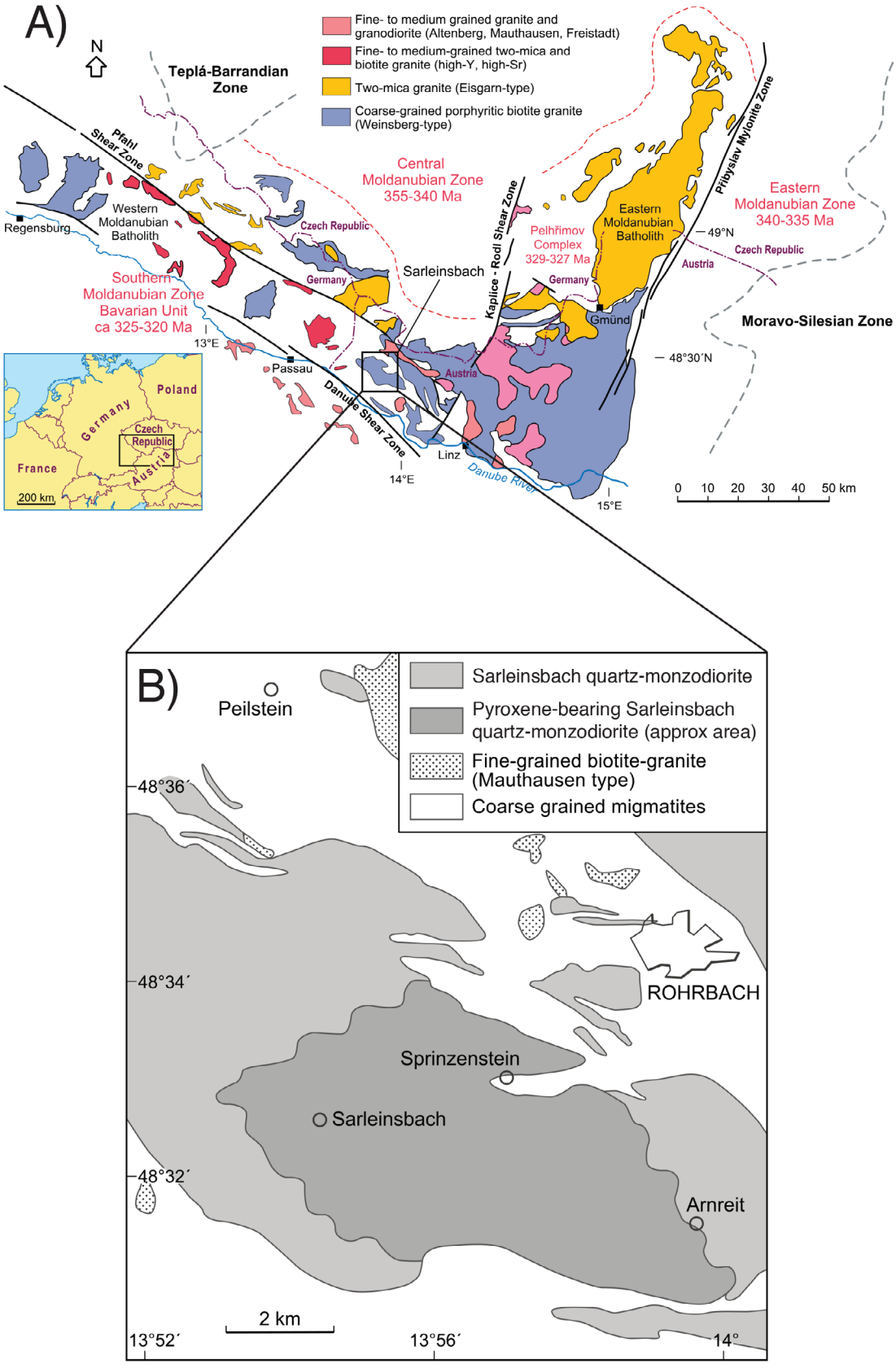

Fig. 1. **A** — Central Moldanubian Zone showing the location of various granite bodies including the Weinsberg granite. **B** — Close-up of the Weinsberg granite where the Sarleinsbach quartz-monzodiorite is located showing the area in which orthopyroxene-bearing (charnockitic) domains can be found as inlayers.

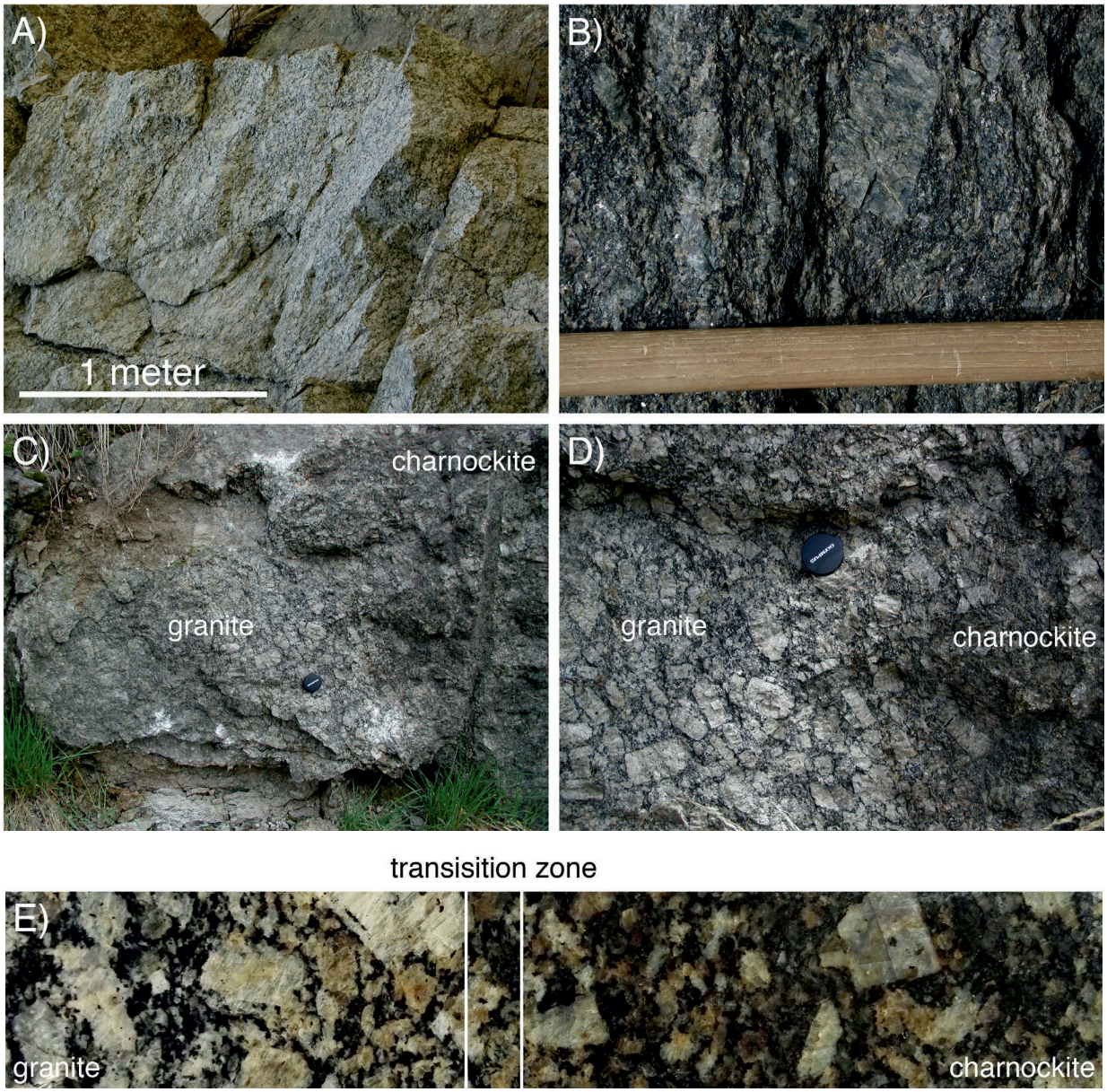

Fig. 2. Field photographs of (**A**) the Weinsberg granite, (**B**) the associated charnockite (orthopyroxene-bearing Sarleinsbach quartz-monzodiorite), (**C**) the boundary between the charnockite and granite, (**D**) a close-up of the contact between the granite and charnockite, and (**E**) a photo of the contact between the granite and charnockite from the polished cross section of a hand sample.

collected and first examined on the petrographic microscope using both transmitted and reflected light and then on the scanning electron microscope (SEM) utilizing high-contrast back scattered electron (BSE) imaging. From this collection, a set of samples was further investigated utilizing electron microprobe (EMP), whole-rock major and trace element analyses, and fluid inclusion microthermometry coupled with Raman analysis.

Whole rock analysis

Large (2–3 kg), fresh and representative samples of charnockite and granite were collected and ground to a fine powder in an agate ball mill. Analyses were conducted by XRF methods on lithium tetraborate glass beads and pressed powder pellets using a Bruker Pioneer S4 crystal spectrometer at the Department for Chemistry and Physics of Materials, University of Salzburg. Obtained net count rates on single X-ray lines were recast into concentration data (wt% and ppm), which is based on an in-house calibration routine that involves measurements of ~30 international geostandards (USGS and GSJ). The calibration is based on the Bruker AXS software SPECTRAplus FQUANT (v1.7) and corrects for absorption, fluorescence, and line overlap effects. Whole rock chemistry results for both the charnockite and granite are given in Table 1. Loss on ignition (LOI) was determined

gravimetrically after heating the dried powders to 1100 °C for three hours.

Electron microprobe (EMP) analysis

Silicate mineral electron microprobe (EMP) analyses of samples from the charnockite were performed using a JEOL JXA-8230 electron microprobe (EMP) with four wavelength-dispersive spectrometers (WDS) at the Center for Global Tectonics, School of Earth Sciences, China University of Geosciences (Wuhan). The operating conditions included a 15 kV accelerating voltage and a 20 nA probe current. Dwell times were 10 s on element peaks and half that on background locations adjacent to peaks. Raw X-ray intensities were corrected using a ZAF (atomic number, absorption, fluorescence) correction procedure. A series of natural and synthetic SPI standards were utilized and changed based on the analysed minerals. An electron beam spot size of 5 μm for K-feldspar (Table 2A) and plagioclase (Table 2B); 1 μm for orthopyroxene (Table 3); and 5 μm for biotite (Table 4) and amphibole (Table 5) was used. Natural and synthetic silicates and oxides, supplied by Structure Probe, Inc (SPI) Supplies (https://www.2spi.com/category/metals-minerals-standards/calibration-eds/), were used for calibration. Standards included albite from Amelia, Virginia, USA; pyrope garnet from Bohemia, Czech Republic; diopside from Wakefield, Quebec, Canada; olivine from a mantle nodule; orthoclase from Madagascar; plagioclase from Sonora, Mexico; and almandine garnet from New York state, USA. Matrix corrections were performed using software supplied by JEOL. In order to ensure that the relative differences observed are correct to within EMP analytical error, all analyses per sample were obtained during one single measuring session including multiple checks of the calibration.

Table 1: Whole rock data.

Sample	**26**	**27**	**28**	**29**	**30**		**31**	**32**	**33**	**34**	**35**	
			charnockite			**mean**			**granite**			**mean**
P_2O_5	0.39	0.52	0.54	0.52	0.44	**0.48**	0.44	0.48	0.51	0.48	0.44	**0.47**
SiO_2	65.97	64.09	63.85	63.47	64.99	**64.47**	64.03	64.92	63.25	64.33	65.84	**64.48**
TiO_2	1.02	1.34	1.37	1.38	1.16	**1.25**	1.26	1.25	1.43	1.22	1.05	**1.24**
SO_3	0.11	0.11	0.11	0.12	0.09	**0.11**	0.10	0.11	0.10	0.11	0.09	**0.10**
Al_2O_3	14.84	15.11	15.08	15.26	15.24	**15.10**	15.34	14.60	15.10	15.15	14.99	**15.04**
Fe_2O_3	4.38	5.41	5.60	5.47	4.29	**5.03**	4.65	5.24	5.37	5.30	4.33	**4.98**
MnO	0.06	0.07	0.09	0.09	0.06	**0.07**	0.09	0.09	0.10	0.08	0.06	**0.08**
MgO	1.22	1.62	1.71	1.65	1.34	**1.51**	1.51	1.66	1.79	1.51	1.37	**1.57**
CaO	3.11	3.69	3.88	3.70	3.22	**3.52**	3.46	3.50	3.59	3.56	3.27	**3.48**
Na_2O	2.91	2.97	3.03	2.97	2.84	**2.94**	2.89	2.84	2.79	3.01	2.94	**2.89**
K_2O	5.33	4.91	4.77	5.10	5.94	**5.21**	5.82	5.00	5.71	5.07	5.30	**5.38**
CO_2	0.20	0.09	0.06	0.06	0.15	**0.11**	0.11	0.13	0.09	0.07	0.14	**0.11**
LOI	0.51	0.28	0.30	0.37	0.40	**0.37**	0.38	0.50	0.30	0.28	0.50	**0.39**
Total	100.05	100.21	100.38	100.15	100.17	100.19	100.08	100.31	100.13	100.19	100.33	100.21
Rb*	160	145	138	147	164	**151**	164	162	155	157	155	**158**
Cs	4	4	4	5	4	**4**	5	6	4	4	5	**5**
Sr	257	264	271	268	278	**268**	275	260	274	264	261	**267**
Ba	1240	1150	1134	1276	1518	**1264**	1376	1089	1407	1201	1256	**1266**
Sc	12	15	16	16	13	**14**	14	15	16	14	12	**14**
Y	25	24	23	25	22	**24**	22	29	22	28	22	**25**
La	40	47	53	60	41	**48**	41	61	42	50	48	**48**
Ce	98	103	122	123	94	**108**	88	135	87	115	111	**107**
Nd	52	62	68	70	54	**61**	53	73	56	65	57	**61**
Zr	436	458	450	430	376	**430**	361	454	416	500	391	**424**
Nb	22	25	26	26	21	**24**	23	27	25	25	21	**24**
V	92	111	116	116	98	**107**	97	99	115	102	89	**100**
Cr	25	30	29	31	26	**28**	31	36	35	28	58	**38**
Co	10	11	12	13	10	**11**	9	10	11	11	10	**10**
Ni	7	8	9	8	7	**8**	6	7	8	8	7	**7**
Cu	19	21	21	20	17	**20**	19	22	19	21	18	**20**
Zn	82	98	100	108	82	**94**	90	96	99	99	80	**93**
Ga	21	22	24	23	22	**22**	23	22	23	22	22	**22**
Pb	32	31	28	31	33	**31**	35	32	31	30	32	**32**
Th	11	12	14	15	9	**12**	11	25	6	15	12	**14**
U	3	4	3	2	1	**3**	3	5	3	4	4	**4**
F	744	865	896	879	839	**845**	892	890	921	846	816	**873**
Cl	172	171	161	173	159	**167**	177	200	178	182	193	**186**

*ppm

Table 2A: Mean K-feldspar analyses.

Sample	# pts	SiO_2	Al_2O_3	FeO	CaO	BaO	Na_2O	K_2O	Total	X_{Kfs}	X_{Ab}	X_{An}	X_{Ba}
WGBT-1	25	64.00	18.20	0.05	0.33	0.30	0.84	16.08	99.80	0.907	0.072	0.016	0.005
		0.24	*0.53*	*0.03*	*0.02*	*0.06*	*0.08*	*0.21*					
WGBT-2	15	64.52	18.05	0.02	0.03	0.43	0.75	16.42	100.22	0.927	0.064	0.001	0.007
		0.51	*0.96*	*0.02*	*0.02*	*0.06*	*0.10*	*0.20*					
WGBT-3	15	63.97	18.18	0.03	0.01	0.80	0.64	16.42	100.05	0.930	0.055	0.000	0.014
		0.27	*0.86*	*0.03*	*0.01*	*0.20*	*0.16*	*0.30*					
WGBT-4	15	63.95	17.87	0.02	0.05	0.60	0.88	16.23	99.59	0.912	0.075	0.002	0.010
		0.33	*0.76*	*0.02*	*0.14*	*0.18*	*0.98*	*1.57*					
WGBT-5a	17	63.44	17.47	0.02	0.03	0.65	0.93	15.93	98.47	0.907	0.081	0.001	0.011
		0.56	*1.16*	*0.02*	*0.02*	*0.18*	*0.57*	*0.88*					
WGBT-5b	15	63.97	18.76	0.02	0.07	0.40	1.70	14.97	99.89	0.844	0.146	0.003	0.007
		0.33	*0.13*	*0.03*	*0.04*	*0.09*	*0.60*	*0.91*					
WGBT-7	11	63.43	18.08	0.02	0.02	0.92	0.63	16.21	99.31	0.928	0.055	0.001	0.016
		0.26	*1.09*	*0.02*	*0.02*	*0.44*	*0.25*	*0.53*					
WG-8	16	63.63	18.49	0.02	0.01	0.56	0.67	16.51	99.88	0.933	0.057	0.000	0.010
		0.60	*1.09*	*0.02*	*0.01*	*0.25*	*0.12*	*0.49*					
WG8/89	17	63.32	18.14	0.05	0.12	0.69	1.60	14.93	98.84	0.845	0.137	0.006	0.012
		0.35	*0.34*	*0.14*	*0.07*	*0.11*	*0.30*	*0.53*					
WG41/90	20	63.23	17.59	0.02	0.05	0.82	0.83	16.05	98.60	0.912	0.071	0.002	0.014
		0.48	*1.04*	*0.02*	*0.07*	*0.16*	*0.17*	*0.29*					
H92	19	63.87	18.27	0.02	0.05	0.91	0.95	15.85	99.93	0.900	0.082	0.002	0.016
		0.46	*1.19*	*0.02*	*0.03*	*0.11*	*0.08*	*0.15*					

Values in italics are the standard deviation for the mean value; Kfs – K-feldspar, Ab – albite, An – anorthite, Ba – celsian.

Table 2B: Mean plagioclase analyses.

Sample	# pts	SiO_2	Al_2O_3	FeO	CaO	BaO	Na_2O	K_2O	Total	X_{Kfs}	X_{Ab}	X_{An}	X_{Ba}
WGBT-1	25	60.62	23.56	0.08	6.92	0.04	7.00	0.44	98.65	0.026	0.630	0.344	0.001
		0.62	*0.85*	*0.02*	*0.41*	*0.03*	*0.24*	*0.07*					
WGBT-2	15	61.21	23.96	0.07	6.79	0.03	7.20	0.26	99.53	0.015	0.647	0.337	0.001
		0.59	*1.05*	*0.03*	*0.41*	*0.03*	*0.27*	*0.07*					
WGBT-3	14	60.76	23.34	0.07	6.91	0.04	7.16	0.33	98.61	0.020	0.639	0.341	0.001
		0.53	*0.49*	*0.02*	*0.39*	*0.03*	*0.25*	*0.09*					
WGBT-4 Plg 1	9	60.86	23.23	0.03	6.46	0.02	7.50	0.20	98.29	0.012	0.669	0.319	0.000
		0.99	*1.33*	*0.02*	*0.71*	*0.02*	*0.41*	*0.04*					
WGBT-4 Plg 2	5	64.48	20.97	0.03	3.94	0.04	9.03	0.10	98.59	0.006	0.801	0.193	0.001
		0.39	*0.44*	*0.02*	*0.37*	*0.02*	*0.21*	*0.03*					
WGBT-5a	20	60.26	22.99	0.09	6.78	0.03	7.07	0.34	97.56	0.020	0.640	0.339	0.001
		0.45	*1.06*	*0.05*	*0.25*	*0.02*	*0.19*	*0.10*					
WGBT-5b	15	61.13	25.55	0.06	6.46	0.03	7.27	0.26	100.76	0.016	0.660	0.324	0.000
		0.48	*0.24*	*0.03*	*0.11*	*0.03*	*0.10*	*0.09*					
WGBT-7	20	60.05	22.90	0.13	6.94	0.03	7.03	0.25	97.33	0.015	0.637	0.347	0.000
		0.30	*0.56*	*0.18*	*0.28*	*0.03*	*0.25*	*0.08*					
WG-8	17	60.42	23.64	0.05	7.12	0.03	7.03	0.28	98.55	0.016	0.630	0.353	0.001
		0.93	*0.64*	*0.02*	*0.60*	*0.04*	*0.36*	*0.04*					
WG8/89	13	60.94	22.36	0.07	8.10	0.03	7.43	0.37	99.30	0.020	0.611	0.368	0.000
		0.63	*0.50*	*0.03*	*0.30*	*0.03*	*0.22*	*0.06*					
WG41/90	19	59.98	23.33	0.07	8.14	0.03	7.01	0.31	98.87	0.017	0.599	0.384	0.001
		0.67	*0.29*	*0.05*	*0.56*	*0.04*	*0.33*	*0.09*					
H92	16	60.29	23.18	0.09	7.85	0.03	6.46	0.39	98.28	0.023	0.584	0.392	0.001
		0.83	*0.49*	*0.03*	*0.61*	*0.03*	*0.35*	*0.10*					

Values in italics are the standard deviation for the mean value; Kfs – K-feldspar, Ab – albite, An – anorthite, Ba – celsian.

EMP analyses of fluorapatite (Table 6) were made on a JEOL JXA-8500F Hyperprobe at the Deutsches GeoForschungs-Zentrum Potsdam, equipped with a thermal field emission gun. EMP operating conditions were 20 kV, 20 nA, and a 15 μm electron beam spot. Additional information regarding the EMP technique used, including counting times, background subtraction, and analysing crystals, can be found in Åmli & Griffin (1975), Williams et al. (2006), Hansen & Harlov (2007), and Förster et al. (2012). Primary standards consisted of synthetic (Y+REE) phosphates prepared by Jarosewich &

Boatner (1991), and natural minerals such as the Durango fluorapatite, and synthetic oxides for other elements. The analytical errors depend on the absolute abundances of each element. Relative errors are estimated to be <1 % at the >10 wt% level, 5–10 % at the 1 wt% level, 10–20 % at the 0.2 to 1 wt% level, and 20–40 % at the <0.1 wt% level. Detection limits were ca. 200 to 300 ppm for all elements analyzed. EMP measurements of Cl and F in fluorapatite were made according to guidelines outlined in Stormer et al. (1993) and Goldoff et al. (2012).

Microthermometry

Phase transitions in fluid inclusions were investigated by using a Linkam THMS 600 heating-freezing stage cooled with liquid nitrogen at the Geowissenschaftliches Zentrum der Universität Göttingen (Shepherd 1981). Samples were prepared as unmounted, doubly polished sections, with an average thickness of 0.2 mm. Because of the low fluid inclusion abundance we prepared two fluid inclusion plates of each sample. The stage was calibrated by a set of synthetic fluid inclusion standards. For temperatures around −56.6 °C (the melting point of CO_2) and around 0 °C, the accuracy is better than ±0.5 °C, whereas for temperatures between 200 and 600 °C, the accuracy is better than ±0.5 °C.

Raman analysis

Raman analysis has been performed with a Horiba-Jobin-Yvon HR-Raman spectrometer provided with a 488 nm (blue) Laser in order to analyse the gas composition of the fluid inclusions. Most samples show Raman shift peaks for CO_2 (diad at 1388 and 1285 cm^{-1}), N_2 (2331 cm^{-1}), and CH_4 (2917 cm^{-1}). Due to pressure and mixing effects, peak positions are downshifted with some wave numbers. The gas compositions were calculated from peak integrals and the Plazcek equation with relative Raman cross-sections of 2.5 (sum of CO_2 diad), 1.0 (N_2), and 7.6 (CH_4) (see Burke 2001).

Whole rock data

Samples of the Weinsberg granite and the associated orthopyroxene-bearing (charnockite) Sarleinsbach quartz-monzodiorite were analysed (Fig. 1B). All samples were taken from a narrow area east of the village of Sprinzenstein (Fig. 1B). It can be seen from Table 1 that both rock types yield a slight internal variability (e.g., SiO_2 63–66 wt%, Fe_2O_3 4.3–5.6 wt%). However, on average, no significant geochemical differences are apparent. Even though the normal granite looks lighter in the hand specimen or in outcrop, its mafic appearance, and SiO_2 content are, on average, the same as in the darker looking charnockite (Fig. 2). Also, there is no significant difference in the other major elements, the trace element contents, or the CO_2 and Cl contents (Table 1).

Finger & Clemens (1995, 2002) interpreted the charnockite as a cumulative magma, which is more mafic compared to the Weinsberg granite in other areas of the batholith. The same interpretation should hold true for the granite from the sampling area, as it is geochemically identical to the charnockite. The reason for why the orthopyroxene is present in one case and absent in the other can thus not be explained by a difference in the major-element, whole-rock composition. It must lie in a reduced H_2O activity in the magma responsible for the charnockite as a function of P–T–X, which shifted the equilibrium represented by reaction (1) into the orthopyroxene stability field.

Mineralogy and petrography

In general the mineralogy, petrology, and geochemistry of the Weinsberg granite and associated orthopyroxene-bearing (charnockite) Sarleinsbach quartz-monzodiorite are the same. The only real difference is the presence of orthopyroxene ±clinopyroxene and its associated biotite-quartz reaction textures in the charnockite and the fact that the K-feldspar megacrysts in the granite are white microcline whereas in the charnockite the K-feldspar is a dark grey, glassy orthoclase with only some partial conversion to microcline.

In the diagram for charnockitic rocks by Streckeisen (1976), the charnockite can be classified as a quartz-jotunite (=hypersthene quartz-monzodiorite after IUGS 1989). The fine-grained pyroxene-bearing domains are mangerite to jotunite to quartz-jotunite (=hypersthene monzonite, hypersthene quartz-monzonite to hypersthene quartz-monzodiorite). According to the Streckeisen-diagram for granitic rocks, the charnockite marks the lower quartz-poor and plagioclase-rich end of the continuous Weinsberg granite trend.

The euhedral to subhedral blocky, dark grey, semi-translucent K-feldspar megacrysts from the charnockite are around 3 cm long, but can exceed 7 cm (Table 2A). The megacrysts consist of orthoclase, which are an uncommon characteristic of the southern Bohemian Batholith (Frasl & Finger 1988). In the dark medium-grained to coarse-grained groundmass, the black biotites are easily visible; quartz and plagioclase measure only a few mm. Microscopically the K-feldspar megacrysts (orthoclase to weak microcline) sometimes contain inclusions of euhedral plagioclase and subhedral orthopyroxene. Biotite inclusions are scarce. Weak perthitic exsolutions occur locally. Broad myrmekitic reaction rims occur at the contacts between K-feldspar and plagioclase (Abart et al. 2014; Fig. 3B). The presence of these myrmekitic rims is generally considered to indicate the presence of low H_2O activity fluids (CO_2-rich and/or saline to hypersaline) along feldspar mineral grain boundaries (cf. Perchuk et al. 2000).

Plagioclase (as andesine), occurs as inclusions in the K-feldspar, as well as grains in the groundmass (up to 7 mm), shows no or weak normal zoning, and is moderately albitic (Ab60–An80) (Table 2B). The higher An-contents form a core region

with speckled extinction. Small, brown, translucent flakes of ilmenite are abundant. Antiperthitic exsolution in the plagioclase can occur as well. The interstitial quartz (ca. 3 mm) forms pavement-like subgrains. Application of the ternary feldspar thermometer of Fuhrman & Lindsley (1988) to co-existing plagioclase and K-feldspar gave only retrograde temperatures of around 600 °C or less.

The subhedral orthopyroxenes (0.2–10 mm) show numerous secondary reaction textures and are relatively Fe-rich (X_{Fe}=0.56–0.66) (Table 3; Fig. 3). Orthopyroxene grains are

Table 3: Mean orthopyroxene analyses.

Sample	# pts	SiO_2	TiO_2	Al_2O_3	Cr_2O_3	FeO	MgO	MnO	CaO	Na_2O	Total	X_{Fe}	X_{Mg}	X_{Mn}	X_{Al}
WGBT-1	24	50.31	0.13	0.37	0.01	38.07	10.53	0.80	1.00	0.01	101.22	0.660	0.326	0.014	0.005
		0.22	*0.06*	*0.05*	*0.01*	*0.55*	*0.31*	*0.04*	*0.22*	*0.01*					
WGBT-2	26	50.47	0.12	0.90	0.02	37.72	10.69	0.83	0.96	0.01	101.71	0.655	0.331	0.015	0.011
		0.26	*0.03*	*1.01*	*0.02*	*0.27*	*0.23*	*0.04*	*0.13*	*0.01*					
WGBT-3	15	50.48	0.11	0.76	0.01	37.62	10.87	0.81	1.04	0.01	101.71	0.651	0.335	0.014	0.009
		0.19	*0.04*	*0.69*	*0.02*	*0.43*	*0.16*	*0.04*	*0.25*	*0.01*					
WGBT-4	10	52.34	0.06	0.53	0.00	32.94	10.27	1.36	1.06	0.05	98.60	0.626	0.348	0.026	0.007
		0.87	*0.03*	*0.14*	*0.01*	*0.30*	*0.10*	*0.07*	*0.14*	*0.02*					
WGBT-5a	20	49.90	0.11	0.27	0.01	37.89	10.86	0.76	1.03	0.01	100.86	0.653	0.334	0.013	0.003
		0.31	*0.03*	*0.04*	*0.01*	*0.44*	*0.20*	*0.05*	*0.26*	*0.01*					
WGBT-5b	15	49.97	0.09	0.34	0.01	37.27	11.03	0.79	0.86	0.01	100.36	0.646	0.341	0.014	0.004
		0.30	*0.03*	*0.08*	*0.01*	*0.53*	*0.24*	*0.04*	*0.20*	*0.01*					
WGBT-7	17	50.23	0.11	2.56	0.02	36.85	10.97	0.75	1.05	0.02	102.56	0.645	0.342	0.013	0.031
		0.57	*0.03*	*0.26*	*0.02*	*0.61*	*0.32*	*0.06*	*0.30*	*0.01*					
WGBT-8/89	20	49.58	0.10	0.99	0.02	35.42	12.74	0.89	0.89	0.01	100.63	0.600	0.385	0.015	0.012
		0.66	*0.03*	*0.84*	*0.02*	*0.20*	*0.16*	*0.04*	*0.08*	*0.01*					
WG41/90	10	52.85	0.06	0.60	0.01	32.42	10.73	1.21	0.93	0.04	98.85	0.614	0.363	0.023	0.008
		0.23	*0.05*	*0.49*	*0.01*	*0.58*	*0.33*	*0.05*	*0.33*	*0.02*					
WG41/90-Cpx	8	52.08	0.12	0.69	0.01	18.17	8.93	0.57	19.60	0.22	100.38	0.524	0.459	0.017	0.014
		0.58	*0.03*	*0.08*	*0.01*	*0.75*	*0.11*	*0.05*	*0.76*	*0.02*					
H92	20	52.16	0.17	0.98	0.02	33.57	14.21	0.85	0.82	0.01	102.79	0.562	0.424	0.014	0.012
		0.55	*0.26*	*0.45*	*0.02*	*0.35*	*0.27*	*0.06*	*0.11*	*0.01*					

Values in italics are the standard deviation for the mean value.

Table 4: Mean biotite analyses.

Sample	# pts	SiO_2	TiO_2	Al_2O_3	FeO	MnO	MgO	BaO	K_2O	Na_2O	F	Cl	H_2O*	sum	O=(F+Cl)	Total	X_{Fe}	X_{Mg}
WBGT-1	15	36.42	5.25	13.00	23.77	0.07	7.91	0.27	9.72	0.05	0.77	0.12	3.04	100.39	0.35	100.04	0.628	0.372
		0.82	*0.20*	*0.10*	*0.35*	*0.02*	*0.14*	*0.07*	*0.10*	*0.02*	*0.19*	*0.01*						
WBGT-2	15	36.61	5.00	13.03	23.89	0.09	7.66	0.20	9.54	0.06	0.64	0.12	3.16	100.01	0.30	99.72	0.636	0.364
		0.32	*0.23*	*0.23*	*0.55*	*0.02*	*0.20*	*0.05*	*0.18*	*0.03*	*0.17*	*0.01*						
WBGT-3	15	36.57	4.51	13.18	24.86	0.08	7.56	0.19	9.50	0.07	0.73	0.09	3.09	100.43	0.33	100.10	0.649	0.351
		0.27	*0.46*	*0.19*	*0.31*	*0.03*	*0.30*	*0.08*	*0.13*	*0.03*	*0.21*	*0.01*						
WBGT-4	15	36.17	3.46	13.87	25.36	0.23	7.02	0.22	9.47	0.06	0.58	0.14	3.17	99.75	0.28	99.47	0.669	0.331
		0.37	*0.74*	*0.48*	*0.57*	*0.05*	*0.24*	*0.06*	*0.12*	*0.02*	*0.22*	*0.04*						
WBGT-5a	15	36.56	4.61	13.24	25.21	0.11	6.92	0.23	9.39	0.08	0.53	0.09	3.27	100.22	0.24	99.98	0.672	0.328
		0.42	*0.41*	*0.38*	*0.89*	*0.03*	*0.68*	*0.09*	*0.40*	*0.03*	*0.11*	*0.03*						
WBGT-5b	14	35.61	4.85	13.47	23.61	0.08	7.86	0.22	9.66	0.05	0.76	0.13	3.00	99.29	0.35	98.94	0.628	0.372
		0.58	*0.67*	*0.34*	*0.83*	*0.02*	*0.27*	*0.06*	*0.15*	*0.02*	*0.16*	*0.01*						
WBGT-7	15	36.58	3.71	13.79	24.39	0.11	7.34	0.21	9.56	0.05	0.52	0.09	3.27	99.61	0.24	99.37	0.651	0.349
		0.31	*0.44*	*0.40*	*0.65*	*0.03*	*0.29*	*0.07*	*0.13*	*0.02*	*0.13*	*0.02*						
WG8	15	36.18	4.30	13.87	25.17	0.29	6.62	0.26	9.47	0.06	0.21	0.07	3.59	100.09	0.10	99.98	0.681	0.319
		0.40	*0.31*	*0.18*	*0.35*	*0.02*	*0.12*	*0.07*	*0.40*	*0.03*	*0.12*	*0.01*						
WG8-89	15	36.58	5.42	13.39	22.32	0.10	8.72	0.27	9.69	0.04	0.47	0.09	3.39	100.47	0.22	100.25	0.590	0.410
		0.41	*0.19*	*0.11*	*0.31*	*0.03*	*0.11*	*0.05*	*0.06*	*0.01*	*0.11*	*0.01*						
WG41-90	15	36.06	4.54	13.74	24.50	0.18	6.94	0.24	9.32	0.07	0.28	0.08	3.50	99.46	0.14	99.32	0.664	0.336
		0.46	*0.42*	*0.20*	*0.79*	*0.03*	*0.29*	*0.05*	*0.31*	*0.02*	*0.07*	*0.01*						
H92	15	36.96	5.59	13.33	21.05	0.09	9.69	0.31	9.84	0.04	0.60	0.11	3.29	100.89	0.27	100.61	0.549	0.451
		0.45	*0.24*	*0.09*	*0.28*	*0.02*	*0.17*	*0.03*	*0.08*	*0.02*	*0.17*	*0.02*						

Values in italics are the standard deviation for the mean value; *calculated assuming that the total charge on the anion site is −2.

Table 5: Mean amphibole analyses.

Sample	# pts	SiO_2	TiO_2	Al_2O_3	FeO	MgO	MnO	CaO	Na_2O	K_2O	F	Cl	H_2O*	Sum	O=(F+Cl)	Total	X_{Fe}	X_{Mg}
WBGT-4	13	52.24	0.20	1.97	21.21	9.25	0.49	10.81	0.23	0.17	0.14	0.01	1.84	98.56	0.06	98.50	0.56	0.44
		1.20	*0.12*	*0.81*	*0.75*	*0.55*	*0.07*	*0.25*	*0.09*	*0.07*	*0.12*	*0.00*						
WBGT-7	14	43.22	0.11	10.15	24.72	5.01	0.23	10.62	0.89	1.10	0.11	0.03	1.77	97.96	0.06	97.91	0.73	0.27
		1.89	*0.05*	*1.46*	*0.83*	*0.55*	*0.04*	*0.38*	*0.22*	*0.26*	*0.10*	*0.02*						
WG-8	16	52.96	0.20	1.72	19.98	8.85	0.67	12.69	0.20	0.14	0.06	0.01	1.94	99.41	0.03	99.39	0.56	0.44
		0.94	*0.13*	*0.98*	*1.63*	*0.61*	*0.09*	*3.41*	*0.08*	*0.11*	*0.11*	*0.01*						
WG41/90	15	43.06	0.08	13.01	22.19	4.95	0.32	10.85	0.99	1.47	0.08	0.06	1.84	98.90	0.05	98.86	0.72	0.28
		0.85	*0.05*	*0.74*	*0.49*	*0.42*	*0.03*	*0.17*	*0.07*	*0.15*	*0.09*	*0.04*						

Values in italics are the standard deviation for the mean value; * calculated assuming that the total charge on the anion site is −2.

Table 6: Mean apatite analyses.

Sample	# grains	P_2O_5	SiO_2	SO_2	Y_2O_3	La_2O_3	Ce_2O_3	Pr_2O_3	Nd_2O_3	Sm_2O_3	Gd_2O_3	Dy_2O_3	CaO	SrO	MnO	FeO[a]	Na_2O	F	Cl	H_2O[b]	sum	O=(F+Cl)	total	$(Y+LREE)_2O_3$
WG-8	6	42.29	0.27	0.01	0.17	0.04	0.17	0.03	0.14	0.08	0.13	0.10	55.36	0.03	0.04	0.11	0.03	3.64	0.03	0.13	102.81	1.54	101.27	0.87
		0.71	*0.16*	*0.01*	*0.12*	*0.04*	*0.07*	*0.04*	*0.07*	*0.07*	*0.06*	*0.06*	*0.27*	*0.02*	*0.02*	*0.06*	*0.02*	*0.12*	*0.01*	*0.08*				
WG41/90	6	42.13	0.27	0.01	0.16	0.09	0.28	0.03	0.25	0.09	0.11	0.01	55.05	0.02	0.04	0.22	0.06	3.61	0.03	0.17	102.62	1.53	101.09	1.01
		0.47	*0.07*	*0.01*	*0.06*	*0.04*	*0.12*	*0.02*	*0.11*	*0.06*	*0.06*	*0.01*	*0.31*	*0.02*	*0.02*	*0.05*	*0.02*	*0.21*	*0.01*	*0.14*				
WG8/89	6	42.31	0.30	0.02	0.16	0.16	0.36	0.10	0.32	0.13	0.09	0.06	54.93	0.02	0.03	0.27	0.05	3.55	0.11	0.17	103.16	1.52	101.64	1.38
		0.52	*0.16*	*0.01*	*0.12*	*0.08*	*0.10*	*0.08*	*0.14*	*0.06*	*0.07*	*0.06*	*0.29*	*0.02*	*0.03*	*0.17*	*0.03*	*0.09*	*0.04*	*0.06*				
H92	6	42.41	0.29	0.01	0.06	0.12	0.33	0.03	0.24	0.03	0.01	0.05	55.38	0.01	0.02	0.11	0.03	3.82	0.13	0.03	103.12	1.64	101.48	0.87
		0.48	*0.09*	*0.01*	*0.05*	*0.07*	*0.06*	*0.04*	*0.07*	*0.04*	*0.01*	*0.04*	*0.28*	*0.01*	*0.02*	*0.07*	*0.02*	*0.14*	*0.03*	*0.06*				

Values in italics are the standard deviation for the mean value; a – measured as FeO; b – estimated from charge balance on the halogen site to be −2.

generally associated with large biotites, and have undergone a partial or complete replacement by biotite and quartz symplectites (see Fig. 3A, C). Ilmenite exsolution lamellae, parallel to the cleavage planes, are abundant in many of the orthopyroxene grains. This suggests that at peak P–T, the orthopyroxene once had a much higher Ti content.

Like the orthopyroxene, the biotite is relatively Fe-rich (X_{Fe}=0.55–0.67) with moderate amounts of F (0.2–0.8) and lesser amounts of Cl (0.1) on the H_2O dominated halogen site (Table 4). A high TiO_2 content of 3.7 to 5.6 oxide wt% (Ti=0.206–0.323) indicates that the biotites formed under high grade conditions at temperatures greater than 700 °C (cf. Henry et al. 2005).

Frequent, ca. 10 to 50 µm thick rims of fibrous, secondary cummingtonite are observed either as surrounding the orthopyroxene and/or along cracks in the orthopyroxene replacing it. Green hornblende rims (5 µm thick) frequently can be found surrounding the outermost part of the cummingtonite rim. Both hornblende and cummingtonite are relatively Fe-rich (X_{Fe}=0.6–0.7) with the anion site dominated by H_2O with small amounts of F (0.1) and trace amounts of Cl (0.01–0.06) (Table 5). Sometimes chlorite is also found replacing orthopyroxene. Those orthopyroxene grains with cummingtonite rims, which are included in K-feldspar and plagioclase, usually have thinner hornblende rims than those in the groundmass. Biotite ± amphibole reaction textures associated with orthopyroxene (e.g. Fig. 3C) reflect the cooling P–T history of the charnockite under an increasing H_2O activity via a reversal of Reactions (1) and (2).

Clinopyroxene (X_{Fe}=0.5) is interstitial to plagioclase and orthopyroxene and relatively scarce (Table 3). Contact between orthopyroxene and clinopyroxene is usually interspaced by secondary cummingtonite. The clinopyroxene often contains thin orthopyroxene exsolution lamellae in two distinct crystallographic directions. In addition to rimming the orthopyroxene, biotite grains (up to 5 mm) can also be found interstitially with respect to the feldspars and pyroxenes. Here the grains are often more or less deformed, and contain numerous inclusions of apatite and zircon.

An orthopyroxene–clinopyroxene temperature of 870 °C was estimated from co-existing orthopyroxene and clinopyroxene in sample WG41/90 at 500 MPa using the orthopyroxene–clinopyroxene thermometer of Brey & Köhler (1990). H_2O activities for orthopyroxene-bearing samples (X_{Fe}=0.6) utilizing the assemblage orthopyroxene–biotite–K-feldspar–quartz were estimated to be around 0.8 ± 0.02 at 800 °C and 500 MPa from figure 8 in Frost & Frost (2008), and the EMP analytical data contained in Tables 2A, 3, and 4 for K-feldspar, orthopyroxene, and biotite, respectively.

Euhedral to semi-euhedral fluorapatites are generally magmatically zoned. They occur as inclusions within all mafic minerals, but also within plagioclase, K-feldspar, and quartz. The magmatic zoning is clearly visible in BSE images. The fluorapatite contains minor amounts of Cl (0.03–0.13) and H_2O (0.03–0.17), nominal REE_2O_3 total abundances of 0.9 to 1.4 wt%, and relatively high FeO contents of 0.1–0.3 (Table 6). A high SiO_2 content of 0.3 and a low Na_2O content of 0.03–0.06 indicates that the principle substitution

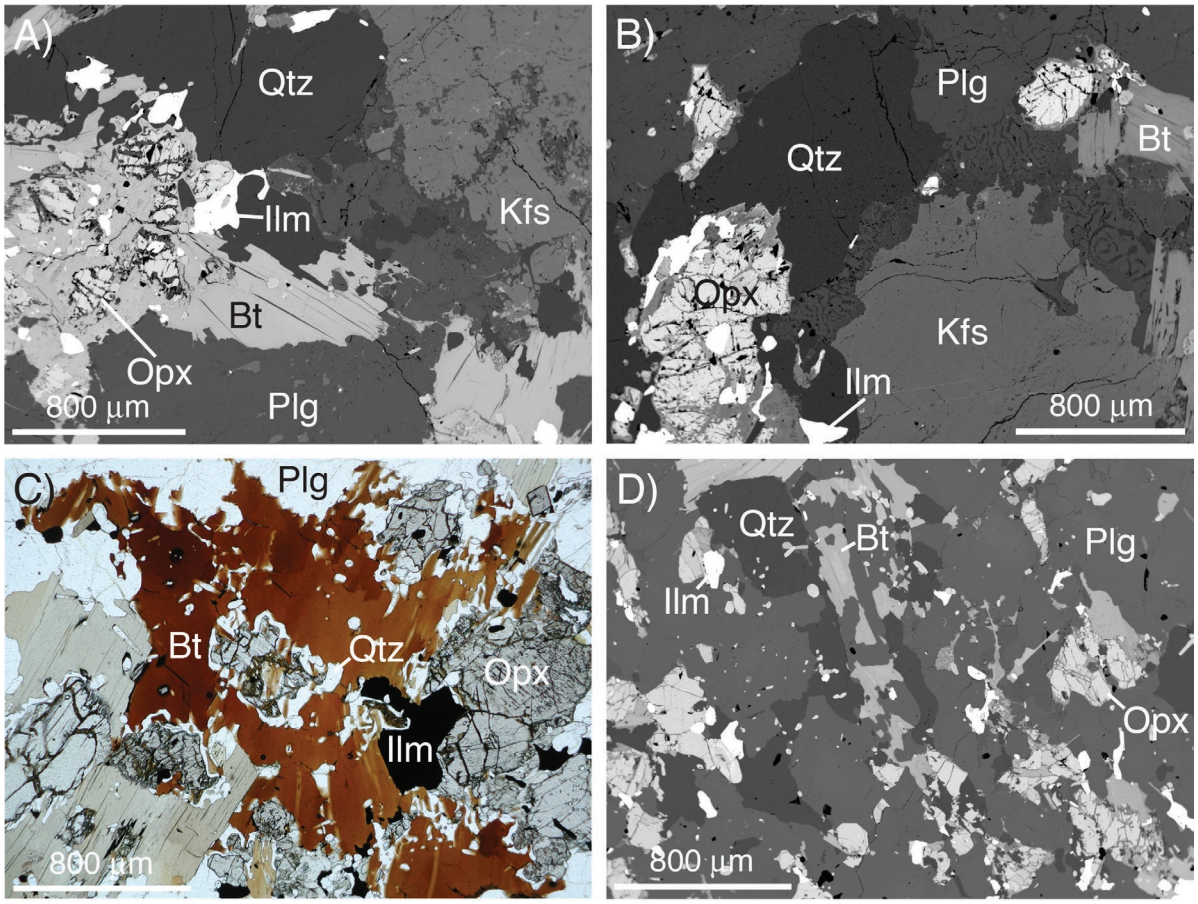

Fig. 3. High contrast BSE images (**A**, **B**, **D**) and a transmitted light image (**C**) of orthopyroxene–biotite–quartz textures from the charnockite.

mechanism for the REE is via the coupled substitution: $REE^{3+}+Si^{4+}=Ca^{2+}+P^{5+}$.

Euhedral zircons with magmatic oscillatory zoning can be found as inclusions in all mineral phases. Two small grains of monazite (<10 µm) have been found in orthopyroxene and K-feldspar. One short prismatic, reddish brown allanite (0.1 mm) was observed along the margin of a plagioclase. Large (>10 µm) primary subhedral ilmenite grains, associated with orthopyroxene, K-feldspar, and plagioclase. Other identified mineral inclusions include pyrite in ilmenite and hematite in biotite.

Fluid inclusion study

Fluid inclusions in the Weinsberg granite and associated orthopyroxene-bearing (charnockite) Sarleinsbach quartz-monzodiorite can be grouped into aqueous inclusions: (1a) biphase aqueous inclusions (Lw+V) with no clathrate observed and (1b) monophase (Lw) aqueous inclusions; (2) aqueous-carbonic inclusions recognized by three or two phases at room temperature (Lw+L+V or Lw+L) and carbonic inclusions; and (3a) monophase or biphase (L+V or L) liquid inclusions and (3b) monophase gas inclusions (V), including "empty" inclusions without observable phase transitions (Fig. 4). The overall majority of the inclusions can be classified as secondary or pseudo-secondary, whereas primary inclusions are relatively rare and restricted to some isolated aqueous-carbonic and high-salinity aqueous inclusions. The inclusion types are similar in both the granite and charnockite, but their relative abundance is very different. Carbonic inclusions make up ca. 43 % in the granite and about 74 % in the charnockite (pie diagram insets in Fig. 4). On the other hand, aqueous inclusions are much more abundant in the granite (ca. 42 %) than in the charnockite (ca. 17 %). The remaining inclusions are aqueous-carbonic (ca. 12±3 % in both lithologies) (Fig. 4). Fluid inclusions occur exclusively in the quartz and have not been found in other minerals like feldspar and pyroxene.

The large variability in shape (equant to irregular); size (from a few microns up to >20 µm); H_2O Vol. Fracs. (full range of zero to 1); and homogenization temperatures (from <100 °C to >400 °C) suggests extensive post-entrapment modifications after first fluid entrapment, particularly in the granite (Fig. 5A–F). Textures and fluid inclusion properties indicate that fluid inclusion modifications include partial H_2O leakage, necking, fluid mixing, and the re-trapping of immiscible fluids during cooling. Fluid inclusions are more

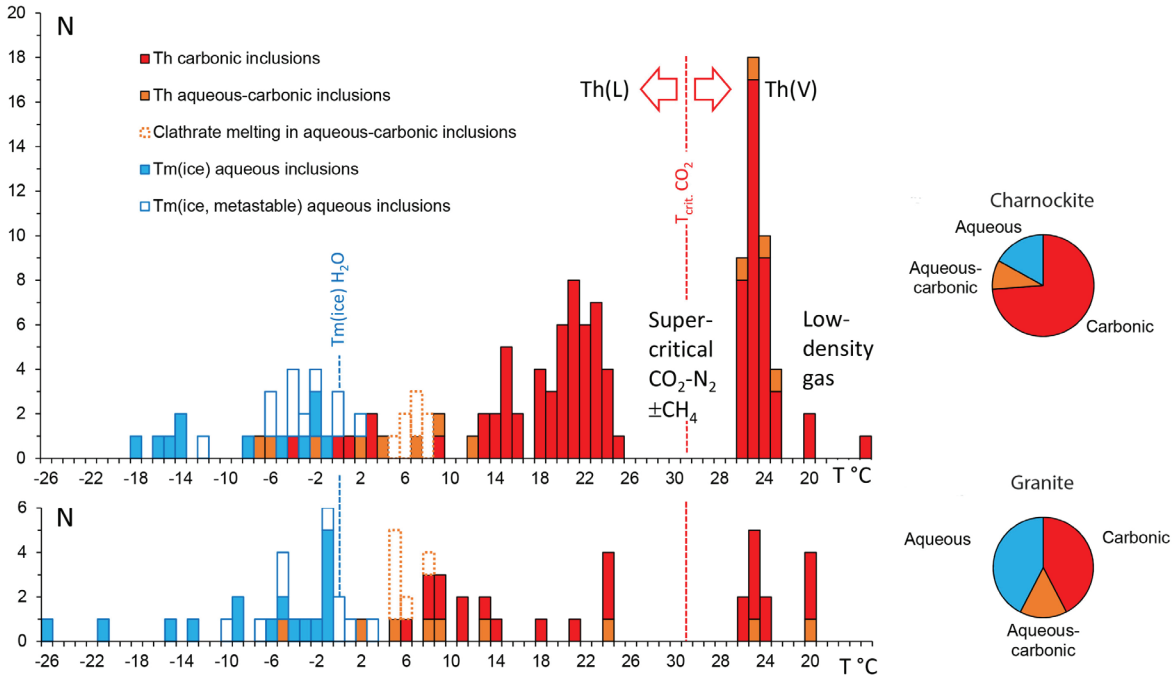

Fig. 4. Fluid inclusion histogram plot for the Weinsberg granite and orthopyroxene-bearing Sarleinsbach quartz-monzodiorite (charnockite). Homogenization temperatures of carbonic and aqueous–carbonic inclusions are marked in red and orange, the final melting temperature of ice and clathrate hydrate in blue and dashed orange, respectively. Tm (ice, metastable) is marked as non-filled blue marks and refers to ice melting in stretched, monophase inclusions (without bubble). A gap of gas homogenizations can be observed between Th=25 °C (L) and Th=27 °C (V) due to the presence of nitrogen and traces of CH_4, which results in supercritical conditions for these mixtures. Estimated relative amounts of gas inclusions, aqueous–gaseous inclusions, and aqueous inclusions are shown as pie-diagrams for both lithologies.

abundant and better preserved in the charnockite compared to the granite.

The large variability in fluid inclusion types within one sample made it difficult to measure total homogenizations at high temperatures as many fluid inclusions decrepitate on heating. Therefore, we could record only a few homogenization temperatures in the high-temperature range, and mainly defined the bulk properties of the fluid inclusions by the estimated H_2O volume fractions combined with the salinity of the solution and the density/composition of the carbonic phase.

Weinsberg granite samples

The granite contains mainly aqueous inclusions of highly varying salinity, whereas gas inclusions are relatively few (Fig. 5A–F; Table 7). Monophase and biphase aqueous inclusions (no gas detected) mainly have low to moderate salinity (healed fractures), but in part very high salinity. The latter are often larger, irregular inclusions trapped in larger, partly healed fractures. The lowest ice melting temperature (Tm) was recorded at −25.3 °C, which corresponds to a salinity of ca. 26 % NaCl-eq. (Fig. 5F; Table 7). Eutectic temperatures (Te) of ca. −48 °C point to a $CaCl_2$-rich composition. These eutectic temperatures could be measured also for inclusions of intermediate salinity, which can be interpreted as diluted $CaCl_2$ solutes.

Many of the aqueous inclusions, however, show very low salinity, or are essentially pure H_2O. These inclusions predominantly occur in healed fractures (trails) (Fig. 5A–F; Table 7). The bubble size of these inclusions is usually very small or they are monophase, which points to low formation temperatures (< ca. 200 °C). Several inclusions loose the bubble on freezing, whereas it re-appears during melting at temperatures above 0 °C (stretched fluids). The H_2O volume fractions of the low-salinity and pure H_2O inclusions are typically higher (smaller or no bubbles) compared to the high-salinity ones (large bubbles). This suggests the late introduction of meteoric water and local fluid mixing at very low temperatures.

Aqueous–gaseous inclusions with demonstrable amounts of gas show highly varying H_2O volume fractions, i.e. from small amounts (H_2O Vol. Frac ca. 0.2) just visible under the microscope, until ca. 0.7 H_2O volume (Fig. 5A–F; Table 7). At room temperature a double meniscus can be observed in a few inclusions, which contain relatively little H_2O. Raman analysis showed that the gas phase of most aqueous–gas inclusions contains CO_2 mostly with substantial amounts of nitrogen (up to 14 mol%); inclusions with the highest H_2O volume fractions of 0.5 to 0.7 have pure nitrogen bubbles (Table 7). The melting of clathrate hydrate could be observed in a number of inclusions between 5 and 9 °C. These temperatures point to the low salinity of aqueous–gaseous inclusions as

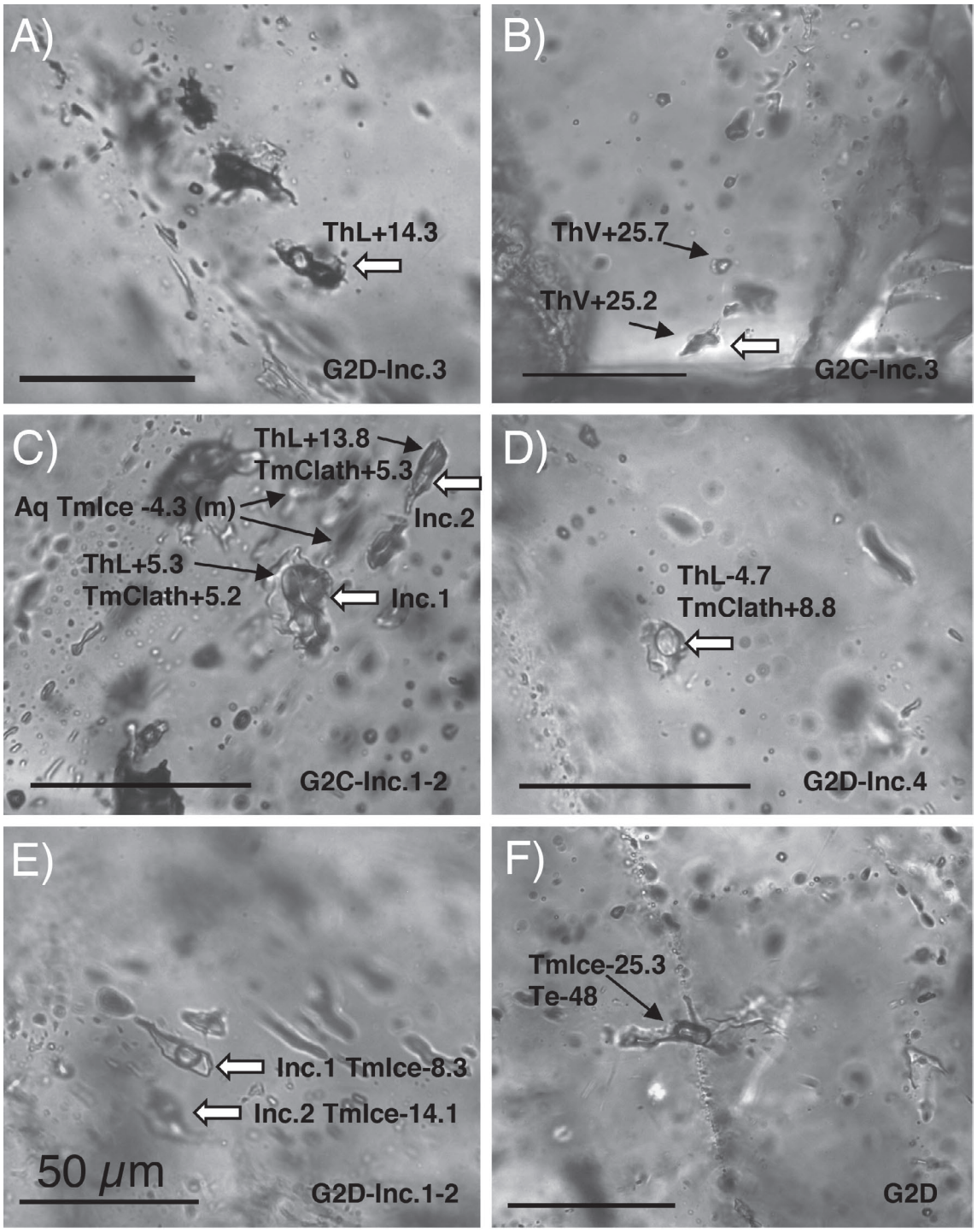

Fig. 5. Fluid inclusion photos. The white arrows point at inclusions, which were measured by Raman analysis and are listed in Table 7. The black scale bar indicates 50 μm in each photo. Photos A–F: Fluid inclusions in quartz from the Weinsberg granite. **A** — Large irregular gaseous inclusions containing CO_2–N_2 mixtures (Table 7). **B** — Aqueous–carbonic (H_2O–NaCl–CO_2) inclusions with H_2O Vol. Frac. of ca. 0.2 (Table 7). **C** — Irregular aqueous–carbonic inclusions (H_2O–NaCl–CO_2–N_2) and aqueous inclusions (Te ca. –30 °C) (Table 7). **D** — Aqueous–carbonic inclusion with high-density CO_2–N_2 phase. H_2O Vol. Frac. ca. 0.6 (Table 7). **E** — Large aqueous inclusions (H_2O–NaCl–N_2) in healed fractures (Table 7). The bubbles contain pure nitrogen. H_2O Vol. Frac.=0.5 to 0.7; Te ca. –23 °C. **F** — Large irregular $CaCl_2$-rich aqueous inclusion with very high salinity. Photos G–K: Fluid inclusions in quartz from the Sarleinsbach quartz-monzodiorite (charnockite). **G** — Low-density carbonic inclusions. Homogenisation is always to the vapour phase or phase transitions have not been observed (Table 7). **H** — Carbonic inclusions ± N_2. **I** — Low-density CO_2–N_2 inclusions showing homogenisation to the vapour phase (Table 7). **J** — Aqueous–gaseous inclusions (H_2O Vol. Frac. ca. 0.4). The gas bubble contains CO_2–N_2 and small concentrations of CH_4 (Table 7). **K** — Aqueous inclusions together with very low-density carbonic inclusions.

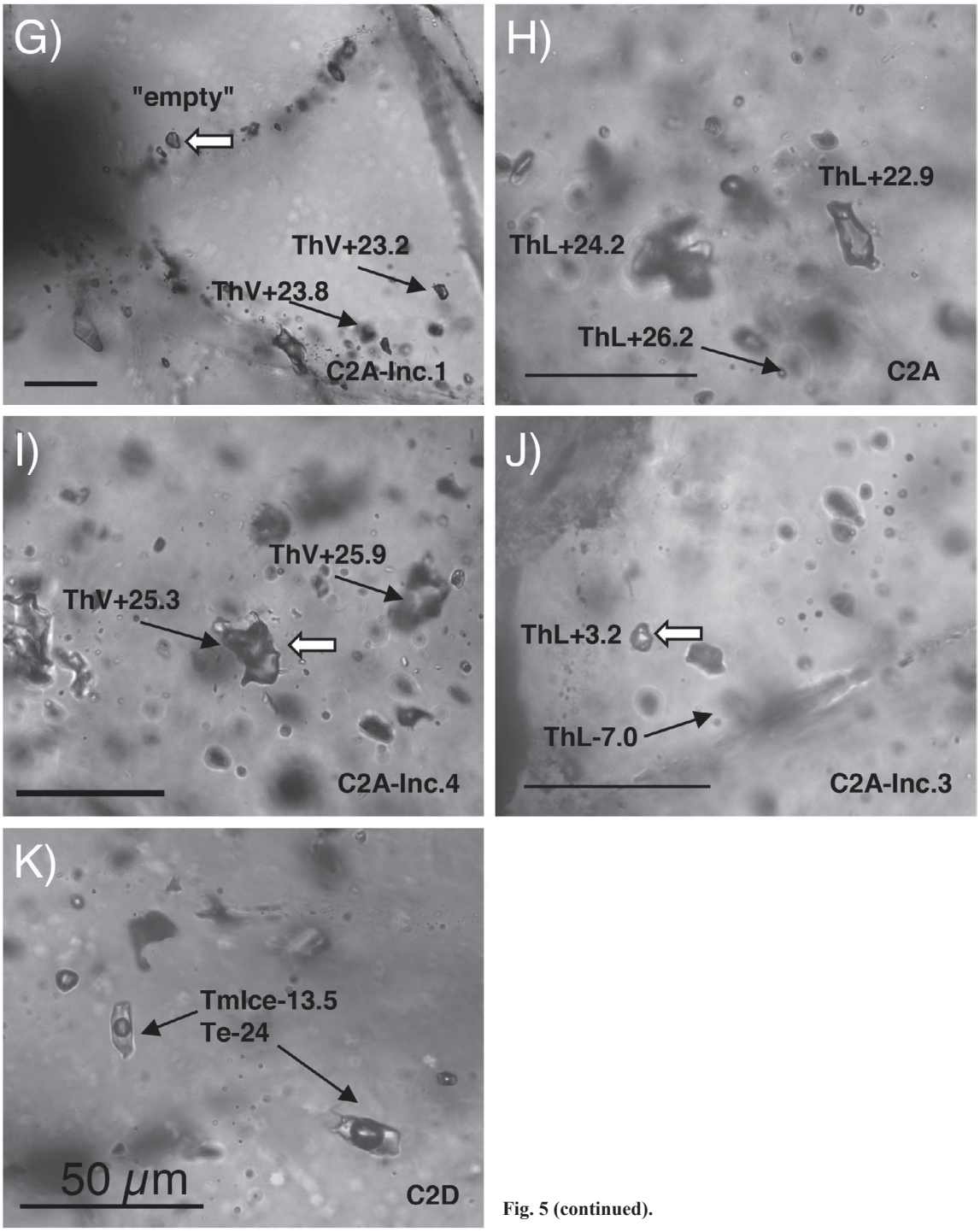

Fig. 5 (continued).

much lower melting temperatures would have been expected for high salinity. Partial homogenisation of the non-aqueous phases is highly variable and may go to the liquid phase at temperatures as low as −5 °C, or to the vapour phase between 20 and 25 °C. Eutectic temperatures are difficult to measure so that the composition of the salt solution is uncertain. Some tests, however, point at NaCl-rich compositions (Te between −20 and −30 °C). Hence the aqueous–gas inclusions can be grouped as two separate populations with either a H_2O–NaCl–CO_2±N_2 or a H_2O–NaCl–N_2 composition.

Gas inclusions, i.e. without demonstrable H_2O, are essentially carbonic in composition, but substantial amounts of nitrogen have been also detected here (Table 7). Homogenisation to the liquid phase ranges from ca. 5 to 25 °C, and to the vapour phase between ca. 20 and 27 °C. L–V homogenisations around 25 °C (L) and 27 °C (V) are about critical. The lowering of the critical temperature confirms the presence of around 10 mol% N_2 in the carbonic inclusions. Also the lack of homogenisation temperatures around 31 °C shows that the carbonic–nitrogen inclusions are supercritical in this

Table 7: Gas compositions as measured by Raman analysis and microthermometry data for selected fluid inclusions. Also listed are the molar volumes of the gas phase as calculated from the equation of state of Thiery et al. (1994).

	Fluid inclusion	Composition	H_2O Vol. Frac.	Th CO_2	Tm CO_2	Tm Ice	Tm clathrate	CO_2	N_2	CH_4	Molar vol. gas *	
Granite (607)												
Fig. 5A	G-2/D inclusion 3	Carbonic (±solid)	0	14.3 L		–	–	91	9	n.d.	55	CO_2–N_2
Fig. 5B	G-2/C inclusion 3	Aqueous–carbonic	0.2	25.2 V		–	–	100	n.d.	n.d.	180	H_2O–NaCl–CO_2
Fig. 5C	G-2/C inclusion 2	Aqueous–carbonic	0.3	13.8 L	−57.4	n.o.	5.4	93.9	6.1	n.d.	54	H_2O–NaCl–CO_2–N_2
Fig. 5C	G-2/C inclusion 1	Aqueous–carbonic	0.3	5.3 L	−58.4	n.o.	5.2	86.2	13.7	0.1?	53	H_2O–NaCl–CO_2–N_2
Fig. 5E	G-2/D inclusion 2	Aqueous–gas	0.5	–	–	−14.1	n.o.	n.d.	100	n.d.	>>	H_2O–NaCl–N_2
Fig. 5D	G-2/D inclusion 4	Aqueous–carbonic	0.6	−4.7 L	−58.1	n.o.	8.8	91.1	8.8	0.1?	49	H_2O–NaCl–CO_2–N_2
Fig. 5E	G-2/D inclusion 1	Aqueous–gas	0.7	–		−8.3	n.o.	n.d.	100	n.d.	>>	H_2O–NaCl–N_2
Charnockite (609)												
Fig. 5G	C-2/A inclusion 1	Low density carbonic	0	n.o.		–	–	100	n.d.	n.d.	>>	CO_2 "empty"
Fig. 5I	C-2/A inclusion 4	Low density carbonic	0	25.3 V		–	–	94.5	5.5	n.d.	201	CO_2–N_2
	C-2/D inclusion 1	Low density carbonic (±solid)	0	24.7 V	−57.2	–	–	91.1	8.3	0.6	209	H_2O–NaCl–CO_2–N_2±CH_4
	C-2/C inclusion 1	Carbonic	0	23.8 L		–	–	89.7	9.7	0.6	60	H_2O–NaCl–CO_2–N_2±CH_4
Fig. 5J	C-2/A inclusion 3	Aqueous–carbonic	0.4	3.2 L		n.o.	n.o.	92.6	6.2	1.2	52	H_2O–NaCl–CO_2–N_2±CH_4
	C-2/A inclusion 2	Aqueous–carbonic	0.6	13.6 L		n.o.	6.4	90.1	9.1	0.8	55	H_2O–NaCl–CO_2–N_2±CH_4

* calculated using the equation of state from Thiery et al. (1994); L – liquid; V – vapor; Th – homogenization temperature; Tm – melting temperature; n.d. – not detected (Raman); n.o. – not observed; '–' – not relevant for the given composition; blank – not measured; >> – molar volume larger than 250 cm^3/mole.

temperature range. Many inclusions in trails do not show phase transitions on cooling and are considered to be very low-density gas ("empty"). The lowest Th for inclusions homogenising to vapour is mainly restricted to the difficulty of observing small amounts of liquid concentrating along the inclusion rim. We assume that the "empty" inclusions consist of CO_2–N_2 gas as well, with very low density.

Sarleinsbach quartz-monzodiorite (charnockite) samples

The charnockite is characterized by carbonic inclusions, which have in part high density with the lowest Th of −4 °C (Fig. 5G–K; Table 7). This type of inclusions have not been found in the Weinsberg granite samples.In addition, low-density, carbonic inclusions occur, which show homogenisation to gas (V), or no phase transitions ("empty"). The higher-density carbonic inclusions (L) typically occur in clusters, whereas the very-low density carbonic inclusions are mainly trapped along trails, which suggests shear and fluid re-trapping at low temperatures and pressures (Fig. 5G–K; Table 7).

In aqueous–carbonic inclusions, we found that the density of the carbonic phase is typically higher for inclusions with higher H_2O Vol. Fracs, whereas inclusions with very little or no visible H_2O show very low density (homogenization to the gas phase). This suggests that many inclusions must have preferentially lost a part or all of the H_2O by partial H_2O leakage after first entrapment of the aqueous–carbonic fluids (e.g., Bakker & Jansen 1990). The H_2O could have induced the formation of secondary hydrous minerals like biotite and/or chlorite, which is common in the charnockite samples (see above). Only a subset of the aqueous–carbonic inclusions have been preserved as primary inclusions.

High-salinity brines are NaCl-rich (Te of −22 °C) and show concentrations of ca. 18 to 21 wt% NaCl (Tm=−14 to −18 °C). Several of these inclusions show characteristics of being primary, i.e. they are regular, relatively large, and isolated (Fig. 5K; Table 7). Some salt daughter crystals occur incidentally. Aqueous inclusions with high H_2O Vol. Fracs are typically trapped along healed fractures and have a much lower salinity approaching that of pure H_2O. The latter are often monophase inclusions. The inclusions with a higher salinity generally have a lower density (larger bubbles) compared to low-salinity inclusions, which normally contain a small bubble or no bubble. This may point to late mixing with meteoric H_2O.

Summation

The fluid inclusion study showed striking differences between fluids in the different lithologies, e.g. late high-salinity, $CaCl_2$-dominated fluids are found in the granite, but not in the charnockite. This may point to stronger feldspar alteration or albitization in the granite. The gas phase in gaseous and aqueous-gaseous inclusions in the granite and in the charnockite typically show CO_2-rich compositions with up to ca. 10 mol% of N_2, i.e. CO_2–N_2 and H_2O–NaCl–CO_2–N_2 for the granite, and CO_2–N_2 and H_2O–NaCl–CO_2–N_2±CH_4 for the charnockite (Table 7; Fig. 6). In the granite, aqueous–gaseous inclusions (H_2O Vol. Frac. of 0.5 to 0.7) are also found with only N_2 in the bubble (H_2O–NaCl–N_2). Low concentrations (<1.2 mol%) of CH_4 have typically been detected in aqueous–carbonic inclusions in the charnockite, but in the granite CH_4 appeared to be absent (Table 7). The fluid inclusion data overall clearly show that the charnockite contains higher amounts of carbonic inclusions (ca. ¾) compared to the granite (less than half).

The molar volume of the gas phase mostly ranges in a narrow band between 49 and 60 cm^3/mole, independent of the H_2O volume fraction, which ranges from 0 to ca. 0.6 (Fig. 6). This observation was made for the granite as well as for

the charnockite and suggests that the inclusions were trapped or re-trapped as immiscible fluids (heterogeneous trapping). All other inclusions with about the same range of H_2O volume fractions show low-density gas bubbles with molar volumes of >180 cm^3/mole. These latter inclusions must be the result of a late stage re-equilibration due perhaps to partial H_2O leakage at low temperatures.

The observation of high CO_2 densities in the charnockitic aqueous–carbonic inclusions was remarkable and suggests that these inclusion compositions may be the closest to the bulk magmatic fluids. Most of the "pure" carbonic inclusions probably represent fluids, which were retrapped during the latter stages of magmatic crystallization. These late stage processes may be responsible for an internal "re-organization" of the fluids. External fluids were probably restricted to very late meteoric water, observed as monophase pure H_2O inclusions in both the granite and the charnockite. However, it is likely that the overall bulk fluid composition of both lithologies was not affected.

Discussion

Interpretation of the fluid inclusion data

The origin of N_2

The presence of N2 in the Weinsberg granite and associated orthopyroxene-bearing (charnockite) Sarleinsbach quartz-monzodiorite suggests the uptake of considerable amounts of sediments with organic material in the granite melt. However, it cannot be excluded that the N_2 could be of magmatic/mantle origin. Nitrogen has been found at different locations in Variscan rocks of middle Europe. Examples include the eclogites of the Münchberg Gneiss (Klemd et al. 1992) and the KTB deep drilling site on the western rim of the Bohemian Massif (Topp 1993). Here N_2 is always a substantial part of the earliest metamorphic paragneisses in the lower and middle crust. These rocks date to before the formation of granitic melts.

Fluids in the charnockite and the granite

The earliest magmatic fluid can be identified as aqueous–carbonic fluids of intermediate salinity and substantial amounts of N_2 (ca. 10 mol%) (Fig. 4). These inclusions are often isolated and relatively large and regular, which indicate their primary or sub-primary (only slightly modified) character (Fig. 5; Table 7). It has been observed that within one sample the density of the carbonic phase is slightly higher for inclusions with the highest H_2O volume fraction. The latter is a further indication that the H_2O-rich aqueous–carbonic inclusions formed at deeper levels. During cooling and uplift the fluids must have been largely re-trapped in the immiscible state at below ca. 400 °C. Fluid inclusions with highly varying H_2O volume fractions (but always lower than the original H_2O content) formed as a result. This process seems to have played a role in both the granite and charnockite (Fig. 6).

The fact that we observe the highest abundance of carbonic inclusions in the charnockite (Fig. 4) appears to imply that these areas of the granite as a whole were dominated by CO_2 during the late magmatic stage, i.e. $CO_2/H_2O>1$, compared to the surrounding granite where H_2O was the dominant fluid phase, i.e. $CO_2/H_2O<1$. In areas of the granitic melt characterized today by charnockite, the amount of CO_2 was sufficiently high enough to lower the H_2O activity to approximately 0.8 (cf. Frost & Frost 2008). In contrast, fluid inclusion salinities show large ranges in both the granite and the charnockite (Fig. 4). While $CaCl_2$ was mainly found in fluid inclusions from the granite, fluid inclusions in the charnockite mainly contain NaCl-bearing solutions. However, there was not a big difference in the fluid inclusion saline concentrations between the granite and the charnockite (Fig. 4). The implication would then be that CO_2–H_2O was the dominant fluid in the granitic magma and that these fluids were heterogeneous during the latter stages of crystallization with some areas of the melt dominated by H_2O (granite) whereas other areas of the melt were dominated by CO_2 (charnockite). Saline fluids, whether NaCl- or $CaCl_2$-dominated, apparently played little or no role here. The CO_2–H_2O inclusions are typically secondary in character, which speaks against an early origin. This supports the scenario that they were trapped during the later stages of crystallization of the granite and thus reflect the fluid conditions in the crystallizing melt at that time.

Formation of the charnockite domains in the Weinsberg granite

From the fluid inclusion data in this study comparing the Weinsberg granite and associated charnockite, a basic conclusion is that during crystallization the charnockite was CO_2-dominated, which lowered the H_2O activity sufficiently such that orthopyroxene was the stable Fe–Mg silicate phase, whereas the granite was H_2O-dominated such that biotite and (rarely) amphibole were the stable Fe–Mg silicate phases. Similar conclusions have been made for incipient (localized), fluid-induced, solid state charnockitization on the meter scale in granitoid rocks world-wide (see discussion and overview in Harlov et al. 2006) as well as for more regional igneous granitoids where charnockite and granite bodies of the same approximate age have crystallized out together intimately associated with each other. Examples of these regional igneous granitoids include the Varberg–Torpa charnockite–granite association (Harlov et al. 2013), the zoned Kleivan granite, Rogaland igneous province, southwest Norway (Madsen 1977; Petersen 1980), and the Louis Lake batholith, Wind River Range, Wyoming, USA (Frost et al. 2000).

In the case of the Varberg–Torpa charnockite–granite association, investigation of the mineralogy, mineral chemistry, petrology, whole rock data, and fluid inclusions from both the Varberg charnockite and associated Torpa granite allowed Harlov et al. (2013) to conclude that emplacement of

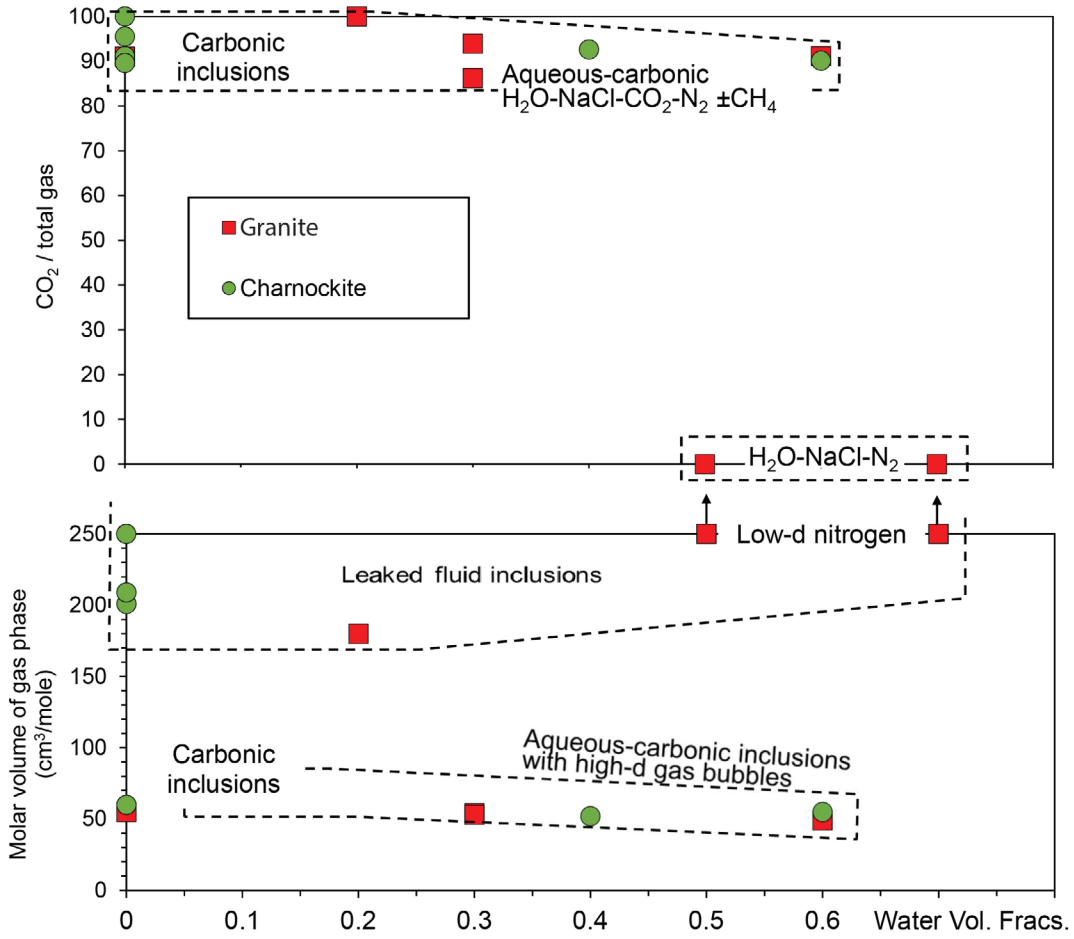

Fig. 6. Fluid inclusion data plots. **A** — The gas composition (CO_2/total gas) plotted against H_2O volume fractions. Note that the Weinsberg granite mainly contains aqueous–carbonic H_2O–NaCl–CO_2–N_2±CH_4 inclusions with a highly variable H_2O content (few "pure" gas inclusions) as well as aqueous–nitrogen inclusions; the Sarleinsbach quartz-monzodiorite (charnockite) contains mainly carbonic inclusions with up to ca. 10 mol% nitrogen and less aqueous–carbonic inclusions. **B** — Molar volumes of the gas phase (cm^3/mole) plotted against H_2O volume fractions. Gas molar volumes fall in a narrow range for gaseous and aqueous–gaseous inclusions, except for "leaked" fluid inclusions which show gas molar volumes of >ca. 180 cm^3/mole.

the charnockite and granite was essentially a two stage process. Namely, that the charnockite crystallized first from a CO_2-rich granitoid magma at 750 to 850 °C and 800 MPa with a sufficiently low H_2O activity, such that orthopyroxene was the stable Fe–Mg silicate. This was followed some 10 to 20 Ma later by the crystallization of the H_2O-rich closely associated and geochemically (whole rock) related amphibole and biotite-bearing Torpa granite at 650 to 700 °C and <700 MPa. This study included the charnockite inliers in the Torpa granite, which are also characterized as being CO_2-rich per the fluid inclusion data (Harlov et al. 2013). The basic conclusion from this study was that the granite and charnockite were derived from a common source magma (most probably a fluid-rich basalt at the base of the crust) as a result of fractional crystallization such that the CO_2-rich, more mafic charnockite was emplaced first followed by the H_2O-rich, more SiO_2-rich granite

The Kleivan batholith consists of a gradual unilateral zonation from charnockite (800 °C) through hornblende granite (775 °C) to biotite granite (690 °C) to a final stage aplite granite (650 °C) (Madsen 1977; Petersen 1980; Jacamon & Larsen 2009). Fluid inclusion work by Madsen (1977) indicates that in the charnockite grading into the hornblende granite, CO_2-rich fluid inclusions are relatively abundant compared to CO_2–H_2O and H_2O fluid inclusions. In contrast, the biotite granite contains almost exclusively H_2O fluid inclusions. CO_2-rich fluid inclusions in the charnockite are interpreted as representing the earliest trapped fluid whereas CO_2–H_2O and H_2O fluid inclusions in the granite are regarded as having been trapped at some later stage after the CO_2-rich fluid inclusions. The H_2O fluid inclusions have high salinities and most likely represent fluids present at a late stage of cracking and healing in the granite. The CO_2–H_2O inclusions represent either early secondary entrapment of a dense

homogeneous CO_2–H_2O fluid or late stage locally heterogeneous mixtures of CO_2 and H_2O. The fluid inclusion data show some similarities with that seen for the Weinsberg granite and associated charnockite domains. The regular mineralogical zoning and geochemical data, coupled with the fluid inclusion data, suggest a three stage fractional crystallization process leading from an orthopyroxene-bearing granite (charnockite) to a hornblende granite; from a hornblende-granite to a biotite granite; and finally from a biotite-granite to an aplite granite. Quantitative modelling by Petersen (1980) indicate that the compositional zonation in the Kleivan granite may have formed by extraction of magma from evolving, more basic, parental magmas deeper in the crust.

The Louis Lake batholith contains units of charnockite within the confines of a granitoid pluton (Frost et al. 2000). The batholith (775–800 °C) is relatively Fe-rich and isotopically has been demonstrated to have formed from a series of different magma sources including a mafic, mantled-derived melt and melts from at least two different crustal sources. In the structurally deepest portion of the batholith (500–600 MPa), the granodioritic and granitic portions contain both orthopyroxene and clinopyroxene. Both pyroxenes gradually grade out going from structurally deeper to shallower levels in the batholith (300 MPa) until only granite and granodiorite remain. Textural and field relationships suggest that this gradation represents, in part, a partial rehydration of the original orthopyroxene- and clinopyroxene-bearing granite and granodiorite during subsolidus cooling implying that the extent of the charnockite bodies within the batholith was once much more extensive. Frost et al. (2000) concluded that charnockite formation within this granitoid body is mostly a matter of areas in the melt with sufficiently low enough H_2O activity (and subsequently a high CO_2 activity) to allow orthopyroxene to be a stable phase. This implies that the original magma was heterogeneous with respect to CO_2 and H_2O.

Similar to these three examples, the Weinsberg granite and associated (magmatic) charnockite is allochthonous and is thought to have originated in the lower crust during a large scale, fluid-absent, melting event associated with the Variscan orogen during the early Upper Carboniferous (Finger & Clemens 1995, 2002; Finger et al. 2003). Finger & Clemens (1995, 2002) considered that the Weinsberg granitic magma (as a whole) originated under granulite-facies conditions through the partial melting of heterogeneous, high-K, biotite-bearing, lower crustal sources, i.e., deep equivalents of the biotite–plagioclase–quartz gneisses of the Mühl zone. The high heat-flow necessary to drive this melting came, most probably, from newly underplated mafic magmas (Finger et al. 2022). However, there is, as yet, no indication that these inferred mafic magmas mixed or mingled with the crustally derived Weinsberg granite magma.

Finger & Clemens (1995, 2002) proposed that the Weinsberg granite and the orthopyroxene-bearing Sarleinsbach quartz-monzodiorite (charnockite), represents a cumulate magma whose crystallisation started within the P–T stability field of orthopyroxene at $T>850$ °C and $P<700$ MPa. This temperature agrees well with an estimated orthopyroxene–clinopyroxene temperature from the charnockite of 870 °C in sample WG41/90 at 500 MPa using the orthopyroxene–clinopyroxene thermometer of Brey & Köhler (1990) and the high Ti content of the biotites (Table 4; Henry et al. 2005). Granites with large K-feldspars, such as the Weinsberg granite, are common in Moldanubian batholiths, from the Massif Central in France to the Bohemian Massif (Fig. 1A) where they are thought to be the product of hot, dry, lower crustal melting, of various metaluminous and peraluminous gneisses (see discussion in Finger & Clemens 1995). Provided that there is enough biotite present to break down and supply the necessary K_2O, the extracted melts will be strongly enriched in K relative to the protoliths.

Other than the necessary low H_2O activity, another important factor that allows orthopyroxene to be a stable phase is the Fe–Mg silicate mineral chemistry. Where measured, the Fe–Mg silicate minerals in all of these examples, including the orthopyroxene-bearing Sarleinsbach quartz-monzodiorite, are relatively Fe-rich (Tables 3–5).Increasing the Fe content extends the stability field for orthopyroxene to higher H_2O activities than that for Mg-rich orthopyroxenes (Frost & Frost 2008, their figure 8). This observation, coupled with the fact that all of these examples are also alkali-rich granitoids, suggest that the chemistry of the melt also played a role in helping to stabilize orthopyroxene (±clinopyroxene) at the P–T of crystallization.

This all presupposes that in the lower crust, there is a CO_2–H_2O component associated with the original granitoid melt. Possible sources for such a component could include contamination by local carbonate rocks, inheritance from the source rock, and/or influx of outside CO_2-rich fluids from some deeper source. In all of these cases, both here and in general, this fluid will invariably contain an NaCl–KCl–$CaCl_2$ component (Brown 2013). Experimentally, it is known that the presence of these salts will enforce a near total immiscibility between CO_2 and H_2O in the fluids associated with the granitoid melt, which would confirm the presence of a CO_2-rich fluid co-existing with an H_2O-rich fluid over the P–T range experienced by these granitoid bodies as melts (Heinrich 2007; Manning 2018). In the current study, the presence of these salts is confirmed by the presence of NaCl and $CaCl_2$ in fluid inclusions from both the Weinsberg granite and the associated charnockite as described above.

In areas of the melt where the CO_2 content is concentrated, such that the H_2O activity is sufficiently lowered, orthopyroxene±clinopyroxene would be the stable Fe–Mg mineral phase during crystallization. In areas of the melt where the CO_2 content is low, such that the H_2O activity approaches or is equal to 1, biotite and amphibole would be the stable Fe–Mg mineral phases. The extent of the corresponding areas of charnockite vs. granite would then be a function of the P–T–X, and the H_2O/CO_2 ratio in the original melt, both during the crystallization of the magma and subsequent cooling and probable uplift. The implication here is that the H_2O/CO_2 ratio is not homogenous in the granitoid melt as a whole, but rather would

be heterogeneous for the reasons given above. If this ratio is dominated by H_2O throughout the melt, most likely only granite or granitoid will crystallize out. If it is dominated by CO_2, magmatic charnockite will form. If both H_2O and CO_2 are present in approximately equal amounts, then granite or granitoid with associated areas of charnockite will crystallize out. This last scenario seems to be what happened in the case of the Weinsberg granite and the orthopyroxene-bearing Sarleinsbach quartz-monzodiorite per the currently known extent of either body. Assuming that this scenario and corresponding hypothesis to be true, then it is highly likely that, other than the examples reported here, there are a certain fraction of the granites and granitoid rocks worldwide with associated orthopyroxene-bearing charnockite bodies or areas/patches, which either have not been discovered, not reported, or have been simply ignored up to the present time. Fluid inclusions from these charnockites should then be dominated by CO_2 as opposed to H_2O in the related granite or granitoid, most likely with a corresponding NaCl–KCl–$CaCl_2$ component.

Acknowledgements: Ning Wen Bin and Timothy Kusky are thanked for helping to obtain the electron microprobe analyses of the silicate minerals at the Center for Global Tectonics, School of Earth Sciences, China University of Geosciences (Wuhan). Friedrich Koller is thanked for showing the first author some of the charnockite patches in the Sarleinsach quartz-monzodiorite as well as for two of the photos in Figure 2. Franziska Wilke is thanked for help with the electron microprobe analysis of apatite at the Deutsches GeoForschungsZentrum. Jacques Touret and a second anonymous reviewer are thanked for their reviews of the paper, which helped to improve it.

References

Abart R., Heuser D. & Habler G. 2014: Mechanisms of myrmekite formation: case study from the Weinsberg granite, Moldanubian zone, Upper Austria. *Contributions to Mineralogy and Petrology* 168, 1074. https://doi.org/10.1007/s00410-014-1074-7

Åmli R. & Griffin W.L. 1975: Microprobe analysis of REE minerals using empirical correction factors. *American Mineralogist* 60, 599–606.

Bakker R.J. & Jansen B.H. 1990: Preferential water leakage from fluid inclusions by means of mobile dislocations. *Nature* 345, 58–60. https://doi.org/10.1038/345058a0

Brey G.P. & Köhler T. 1990: Geothermobarometry in four-phase lherzolites II. new thermobarometers, and practical assessment of existing thermobarometers. *Journal of Petrology* 31, 1353–1378. https://doi.org/10.1093/petrology/31.6.1353

Brown M. 2013: Granite: from genesis to emplacement. *Geological Society of America Bulletin* 125, 1079–1113. https://doi.org/10.1130/B30877.1

Burke E.A.J. 2001: Raman microspectrometry of fluid inclusions. *Lithos* 55, 139–158. https://doi.org/10.1016/S0024-4937(00)00043-8

Clemens J.D. 2012: Granitic magmatism, from source to emplacement: a personal view. *Applied Earth Science (Transactions of the Institute of Mining and Metallurgy B)* 121, 107–136. https://doi.org/10.1179/1743275813Y.0000000023

Finger F. & Clemens J.D. 1995: Migmatization and "secondary" granitic magmas: effects of emplacement and crystallization of "primary" granitoids in Southern Bohemia, Austria. *Contributions to Mineralogy and Petrology* 120, 311–326. https://doi.org/10.1007/BF00306510

Finger F. & Clemens J.D. 2002: Cadomian lower-crustal contributions to Variscan granite petrogenesis (South Bohemian Batholith, Austria): a comment. *Journal of Petrology* 43, 1779–1781. https://doi.org/10.1093/petrology/43.9.1779

Finger F., Doblmayr P., Friedl G., Gerdes A., Krenn E. & Von Quadt, A. 2003: Petrology of the Weinsberg granite in the South Bohemian Batholith: New data from the mafic end members. *Journal of the Czech Geological Society* 48, 46–47.

Finger F., Schiller D., Lindner M., Hauzenberger C., Verner K. & Žák, J. 2022: Ultra high-temperature granites and a curious thermal eye in the post-collisional South Bohemian batholith of the Variscan orogenic belt (Europe). *Geology* 50, 542–546. https://doi.org/10.1130/G49645.1

Förster H.-J., Rhede D., Stein H.J., Romer R.L. & Tischendorf G. 2012: Paired uraninite and molybdenite dating of the Königshain granite: Implication for the onset of late-Variscan magmatism in the Lausitz block. *International Journal of Earth Science* 101, 57–67. https://doi.org/10.1007/s00531-010-0631-1

Frasl G. & Finger F. 1988: Führer zur Exkursion der Österreichischen Geologischen Gesellschaft ins Mühlviertel und in den Sauwald. Reihe Exkursionsführer, Mitteilungen der Österreichischen Geologischen Gesellschaft, 1–30.

Frost B.R. & Frost C.D. 2008: On charnockites. *Gondwana Research* 13, 30–44. https://doi.org/10.1016/j.gr.2007.07.006

Frost B.R., Frost C.D., Hulsebosch T.P. & Swapp S.M. 2000: Origin of the charnockites of the Louis Lake Batholith, Wind River Range, Wyoming. *Journal of Petrology* 41, 1759–1776. https://doi.org/10.1093/petrology/41.12.1759

Fuhrman M.L. & Lindsley D.H. 1988: Ternary-feldspar modeling and thermometry. *American Mineralogist* 73, 201–215.

Gerdes A. 2001: Magma homogenization during anatexis, ascent and/or emplacement? Constraints from the Variscan Weinsberg Granites. *Terra Nova* 13, 305–312. https://doi.org/10.1046/j.1365-3121.2001.00365.x

Goldoff B., Webster J.D. & Harlov D.E. 2012: Characterization of fluor-chlorapatites by electron probe microanalysis with a focus on time-dependent intensity variation of halogens. *American Mineralogist* 97, 1103–1115. https://doi.org/10.2138/am.2012.3812

Hansen E.C. & Harlov D.E. 2007: Whole-rock, phosphate, and silicate compositional trends across an amphibolite- to granulite-facies transition, Tamil Nadu, India. *Journal of Petrology* 48, 1641–1680. https://doi.org/10.1093/petrology/egm031

Harlov D.E., Johansson L., Van den Kerkhof A. & Förster H.-J. 2006: The role of advective fluid flow and diffusion during localized, solid-state dehydration: Söndrum Stenhuggeriet, Halmstad, SW Sweden. *Journal of Petrology* 47, 3–33. https://doi.org/10.1093/petrology/egi062

Harlov D.E., van den Kerkhof A. & Johansson L. 2013: The Varberg-Torpa charnockite-granite association, SW Sweden: mineralogy, petrology, and fluid inclusion chemistry. *Journal of Petrology* 54, 3–40. https://doi.org/10.1093/petrology/egs060

Harlov D.E., van den Kerkhof A. & Johansson L. 2014: Localized, solid-state dehydration associated with the Varberg charnockite intrusion, SW Sweden. *Precambrian Research* 253, 50–62. https://doi.org/10.1016/j.precamres.2014.04.019

Haunschmid B. & Finger F. 1994: Der quarzmonzodiorit von Sarleinsbach: eine kummulatvariante des Weinsberger granits. *Mitteilungen der Österreichischen Mineralogischen Gesellschaft* 139, 310–312.

Heinrich W. 2007: Fluid immiscibility in metamorphic rocks. In: Liebscher A. & Heinrich C. (eds): Fluid-Fluid Interactions. *Reviews in Mineralogy and Geochemistry* 65, 389–430. https://doi.org/10.1515/9781501509407-013

Henry D.J., Guidotti C.V. & Thomson J.A. 2005: The Ti-saturation surface for low-to-medium pressure metapelitic biotites: implications for geothermometry and Ti-substitution mechanisms. *American Mineralogist* 90, 316–328. https://doi.org/10.2138/am.2005.1498

Jacamon F. & Larsen R.B. 2009: Trace element evolution of quartz in the charnockitic Kleivan granite, SW-Norway: The Ge/Ti ratio of quartz as an index of igneous differentiation. *Lithos* 107, 281–291. https://doi.org/10.1016/j.lithos.2008.10.016

Jarosewich E. & Boatner L.A. 1991: Rare-earth element reference samples for electron microprobe analysis. *Geostandards Newsletter* 15, 397–399.

Klemd R., Van den Kerkhof A.M. & Horn E.E. 1992: High-density CO_2–N_2 inclusions in eclogite-facies metasediments of the Münchberg Gneiss complex, SE Germany. *Contributions to Mineralogy and Petrology* 111, 409–419.

Klötzli U.S., Koller F., Scharbert S. & Höck V. 2001: Cadomian lower-crustal contributions to Variscan granite petrogenesis (South Bohemian pluton, Austria): Constraints from zircon typology and geochronology, whole rock, and feldspar Pb–Sr isotope systematics. *Journal of Petrology* 42, 1621–1642. https://doi.org/10.1093/petrology/42.9.1621

Madsen J.K. 1977: Composition and microthermometry of fluid inclusions in the Kleivan granite, south Norway. *American Journal of Science* 277, 673–696. https://doi.org/10.2475/ajs.277.6.673

Manning C.E. 2018: Fluids of the lower crust: deep is different. *Annual Review of Earth and Planetary Sciences* 46, 67–97. https://doi.org/10.1146/annurev-earth-060614-105224

Perchuk L.L., Safonov O.G., Gerya T.V., Fu B. & Harlov D.E. 2000: Mobility of components in metasomatic transformation and partial melting of gneisses: an example from Sri Lanka. *Contributions to Mineralogy and Petrology* 140, 212–232. https://doi.org/10.1007/s004100000178

Petersen J.S. 1980: The zoned Kleivan granite – an end member of the anorthosite suite in southwest Norway. *Lithos* 13, 79–95. https://doi.org/10.1016/0024-4937(80)90065-1

Shepherd T.J. 1981: Temperature-programmable heating-freezing stage for microthermometric analysis of fluid inclusions. *Economic Geology* 76, 1244–1247. https://doi.org/10.2113/gsecongeo.76.5.1244

Stormer J.C. Jr., Pierson M.J. & Tacker R.C. 1993: Variation of F and Cl X-ray intensity due to anisotropic diffusion of fluorapatite during electron microprobe analyses. *American Mineralogist* 78, 641–648.

Streckeisen A. 1976: To each plutonic rock its proper name. *Earth Science Reviews* 12, 1–33. https://doi.org/10.1016/0012-8252(76)90052-0

Thiery R., Van den Kerkhof A.M. & Dubessy J. 1994: vX properties of CH_4–CO_2 and CO_2–N_2 fluid inclusions; modelling for T<31 °C and P<400 bars. *European Journal of Mineralogy* 6, 753–771. https://doi.org/10.1127/ejm/6/6/0753

Topp J. 1993: Flüssigkeitseinschluß-Untersuchungen am Bohrmaterial der KTB bis 4000 Meter. *Göttinger Arbeiten zur Geologie und Paläontologie* 61. PhD Dissertation, University of Göttingen, 1–58.

Williams M.L., Jercinovic M.J., Goncalves P. & Mahan K. 2006: Format and philosophy for collecting, compiling, and reporting microprobe monazite ages. *Chemical Geology* 225, 1–15. https://doi.org/10.1016/j.chemgeo.2005.07.024